5-2007

Searching for H_3^+ in the Atmosphere of the Exoplanet HD 209458b

Matthew Troutman
Clemson University, mtroutm@clemson.edu

SEARCHING FOR H_3^+ IN THE ATMOSPHERE OF THE EXOPLANET HD 209458B

A Thesis
Presented to
the Graduate School of
Clemson University

In Partial Fulfillment
of the Requirements for the Degree
Master of Science
Physics

---

by
Matthew R. Troutman
May 2007

Accepted by:
Dr. Sean D. Brittain, Committee Chair
Dr. Jeremy King
Dr. Mark D. Leising

ABSTRACT

The study of planets outside of the solar system, known as exoplanets, is a very young field. Since the first discovery of an exoplanet in 1992 (and around a solar-type star in 1995), this field in astronomy has garnered much interest. The ultimate goal of discovering life elsewhere in the universe seems to be within reach, despite current technological limitations. First, the limits of current technology need to be found in order to see how limited such observations are using modern telescopes. Second, the atmospheres of exoplanets must be accurately described and modeled. To determine the detection limits, one can study the atmospheres of currently known exoplanets. These exoplanets are typically the mass of Jupiter, but are very close to their host stars, thus typically referred to as "hot" Jupiters. While these are not necessarily cradles of life, they represent advantageous testbeds of exoplanet atmospheres. Observations can constrain models and test the limits of current telescopes.

One such laboratory to test both observational limits and atmospheric models is the exoplanet HD 209458b, a transiting exoplanet. In particular, the molecule H_3^+ is a diagnostic of the thermal regulation in the ionosphere of the exoplanet, and therefore is an advantageous molecule to test both atmospheric models and observational limits. Recent observations of the transiting exoplanet HD 209458b have revealed evidence of sodium in the lower atmosphere and escaping hydrogen, carbon, and oxygen from the exosphere, providing new insight to the composition and physical processes relevant to short-period exoplanets.

The exoplanet HD 209458b was observed using Phoenix on Gemini South in 2005. The observations can constrain the physical conditions and photo-processing of the planet's atmosphere and characterize the gas that may currently be radiatively removed from it, as well as potentially provide insight to the interplay between the

stellar and planetary magnetic fields. The observations represent significant and timely tests for both models of exoplanetary atmospheres and observational limits.

DEDICATION

To Mom, for believing in me, no matter what.

To Dad, for giving me the inspiration to be who I am today.

To Adrienne, for making me want to be the big brother I should be.

ACKNOWLEDGEMENTS

"If I have seen things others have not, it is because I have stood on the shoulders of giants."

I would like to first acknowledge my advisor, Dr. Sean Brittain, for taking on an inexperienced student even before arriving on campus. I am honored to be his first advisee to gain a degree. I hope the remainder of my graduate career will continue to be as fun as the first two.

I wish to acknowledge the other members of my knowledgeable committee: Dr. Jeremy King and Dr. Mark Leising. Thanks for the comments, support, and very helpful questions along the way.

I wish to thank Dr. Terry Rettig at the University of Notre Dame for insightful comments on research proposals and this thesis, as well as support for research form the National Science Foundation under contract AST-0507621.

I would also like to thank the people who put up with me nearly every day. Specific thanks to Kiran, who helped to keep me sane during the long hours of my entire first year. Thanks to Simon, after whom I try to model my work ethic and motivation. Thanks to Allen for being open to any questions: physics, coding, and of course, Futurama. Thanks to Autumn, for helping with SARA observations; it would have been great to work with you longer. Thanks to Keith and Mark, for being open ears at all times. Finally, thanks to the first year students, specifically Ginger and Yu. Your fantastic progress keeps me working harder.

This thesis is primarily based on observations obtained at the Gemini Observatory (program ID GS2005B-C-6), which is operated by the Association of Universities for Research in Astronomy, Inc., under a cooperative agreement with the NSF on behalf of the Gemini partnership: the National Science Foundation (United States), the Particle Physics and Astronomy Research Council (United Kingdom),

the National Research Council (Canada), CONICYT (Chile), the Australian Research Council (Australia), CNPq (Brazil) and CONICET (Argentina).

The NIRSPEC data shown were obtained at the W.M. Keck Observatory (program ID H06aNS), which is operated as a scientific partnership among the California Institute of Technology, the University of California and the National Aeronautics and Space Administration. The Observatory was made possible by the generous financial support of the W.M. Keck Foundation.

TABLE OF CONTENTS

Table of Contents (Continued)

Page

LIST OF TABLES

LIST OF FIGURES

List of Figures (Continued)

CHAPTER 1

INTRODUCTION

Astronomy is full of exciting fields that push the edge of research capabilities. One of these exciting fields is the study of exoplanets, which are planets around stars other than the Sun. Exoplanets are of great interest to the scientific community due to the insight they can provide to the formation and evolution of our own planet, as well as other planets in our solar system. Studies of exoplanets are a relatively young field, with the first discoveries coming in the 1990s using pulsar timing and radial velocity studies of stars. Since then, there have been many more planets detected, with current numbers being over 200 confirmed planets (Butler et al. 2006). Not all have been found using these methods, with some discovered or confirmed through transit studies, microlensing, and most recently, direct observation.

Studies of exoplanets are of great interest for a number of reasons. By studying an exoplanet at different stages of its evolution, information can be gathered about how the planet may have formed or how planets change over time. What is the difference between the formation of a gas giant like Jupiter versus a rocky planet like the Earth? Is the formation of Earth at 1 AU or Neptune at its distance rare or common? These are the types of questions that exoplanetary studies would like to answer.

If important factors to planet formation and planetary evolution can be determined, then we can determine the best ways to search our local neighborhood for candidate stars with exoplanets, possibly even searching for exoplanets similar to Earth. These are all smaller parts of a greater question: is there life elsewhere in the Universe? While this question is too large and difficult to answer in the immediate future, steps can be taken to provide the ability to answer this question directly. Current studies are taking giant leaps with these goals in mind.

The detection of life elsewhere in the Universe will likely be a biomarker in the atmosphere of an exoplanet rather than some sort of "phone call" from ET. However, the detection of a biomarker has many things that need to be considered before this would be possible. If one assumes that life is not possible in a Jovian-like world, then one would need to be able to detect specific molecular signatures in the atmospheres of near Earth-sized exoplanets. Some combination of molecules that would be considered biomarkers (evidence for life) are ozone (O_3), water (H_2O), methane (CH_4), and carbon dioxide (CO_2) (Selsis 2002). Alone, these molecules may be found without life, but the combination would be indicative of life - at least as we know it on Earth.

However, detecting molecular signatures in the atmosphere of an Earth-sized exoplanet presents problems. First, the smallest mass planet discovered to date is 5.5 times greater than the mass of Earth (Beaulieu et al. 2006). This means that detections of smaller-mass planets are necessary before the atmosphere of such a planet is studied. Second, the ability to detect specific molecules in the atmospheres of exoplanets is a new field itself. One particular exoplanet, HD 209458b[1], has been the scrutiny of many studies for atmospheric signatures due to its short orbit and close proximity to the host star. Sodium (NaI) (Charbonneau et al. 2002), Carbon (CI), Oxygen (OI) (Vidal-Madjar et al. 2004), and escaping Hydrogen (HI) (Vidal-Madjar et al. 2003) have all been found in the extended atmosphere of the exoplanet. However, even though HD 209458b is a Jovian-sized planet, no molecules have been detected yet. Thus far, there has not been a ground based detection of an exoplanetary atmospheric signature. Fortunately, with more sophisticated techniques and advanced telescopes, the study of an exoplanetary atmosphere is something that is in the foreseeable future with planned space telescopes such as the Terrestrial Planet Finder (TPF) and Space Interferometry Mission (SIM) from NASA, as well as Darwin from the European Space Agency.

---

[1] HD 209458b was nicknamed "Osiris" by Vidal-Madjar et al. (2004), but for this thesis will be referred to using the catalog name.

The intent of this thesis is to attempt to observe a molecule in the atmosphere of an exoplanet from ground-based observations. Specifically, data from the PHOENIX instrument on Gemini South will be used in an attempt to detect the H_3^+ molecule in the atmosphere of the exoplanet HD 209458b. A detection will be the first detection of a molecule in an exoplanetary atmosphere. A non-detection will put upper limits on the amount of H_3^+ in the atmosphere of HD 209458b and constrain models that predict different column densities in the atmosphere of the exoplanet (i.e. Yelle 2004; Miller et al. 2000).

The organization of the thesis is as follows, in chapter 1: section 1.1 will introduce current, past and future techniques used in the discovery of exoplanets. The scientific motivation for this thesis will be presented in section 1.2. In chapter 2, HD 209458b will be discussed, covering past methods of studies and the specifics of the exoplanet itself. Chapter 3 will discuss the H_3^+ molecule and its importance and relevance to this thesis and exoplanetary studies in general. Chapter 4 will present the data and subsequent analysis. Finally, chapter 5 will discuss future plans for the project.

1.1 Techniques for Exoplanet Detection

Many techniques have been developed and have evolved in the search for exoplanets, each method with its own characteristic advantages and disadvantages, capabilities and limits. The first exoplanets were discovered around pulsars (these were not initially accepted for reasons described in §§1.1.1). Radial velocity measurements of stars have since proved to be the major contributor to the current number of recognized exoplanets, with transit studies, microlensing, and direct observation contributing or confirming to the current count. These search techniques are not mutually exclusive, often extracting more information that may not be accessible through one of the methods. For example, radial velocity studies and transit studies are done on the same star in many cases, allowing the determination of the mass, radius, eccentricity, and size of the orbit of the exoplanet.

Despite being postulated for centuries, the existence of exoplanets was not proven until the early 1990s. This is because the technology needed to confirm the existence of an exoplanet first became available at that time. The first methods used to detect exoplanets - pulsar measurements and radial velocity measurements - both require precise observations and data analysis techniques to detect the small changes that occur in the host star due to the orbiting exoplanet. Even when the orbiting planet is relatively large (on the order of or larger than a Jupiter mass planet), barely measurable changes occur, so improved techniques are needed to detect smaller mass exoplanets. A figure showing the limits of the different techniques is shown in figure 1.1. As the technology improves, masses of exoplanets discovered will become smaller, with the subsequent analysis of them becoming greater.

1.1.1 Pulsar Measurements

Surprisingly, the first exoplanet discovered was around a pulsar (Wolszczan and Frail 1992). Measurements in the regularity of a pulsar determined that another object was in the system that was less massive than a brown dwarf, therefore, a massive planet. This success came after a false positive was reported of a pulsar with a planetary companion having a one year orbit. This was later retracted after it was realized that a correction for Earth's motion was not taken into account. The false positive caused later scientists making discoveries using this method to scrutinize their own data and to be very hesitant to publish results. Pulsar studies were gradually accepted as more successful detections were made. Currently, exoplanets discovered through pulsar measurements have become less common, as pulsars themselves are a rare phenomenon, and pulsars with a planet that has survived the initial catastrophic event of pulsar creation are even less probable. Using pulsar timing, the planet's minimum mass and semi-major axis are determined.

Pulsar studies for exoplanets are currently rare for a few reasons. First, there is little information that can be gained - the exoplanetary mass and semi-major axis. Usually, this is not a problem, but pulsars often are further from Earth than planets found using other techniques and therefore cannot be complimented by

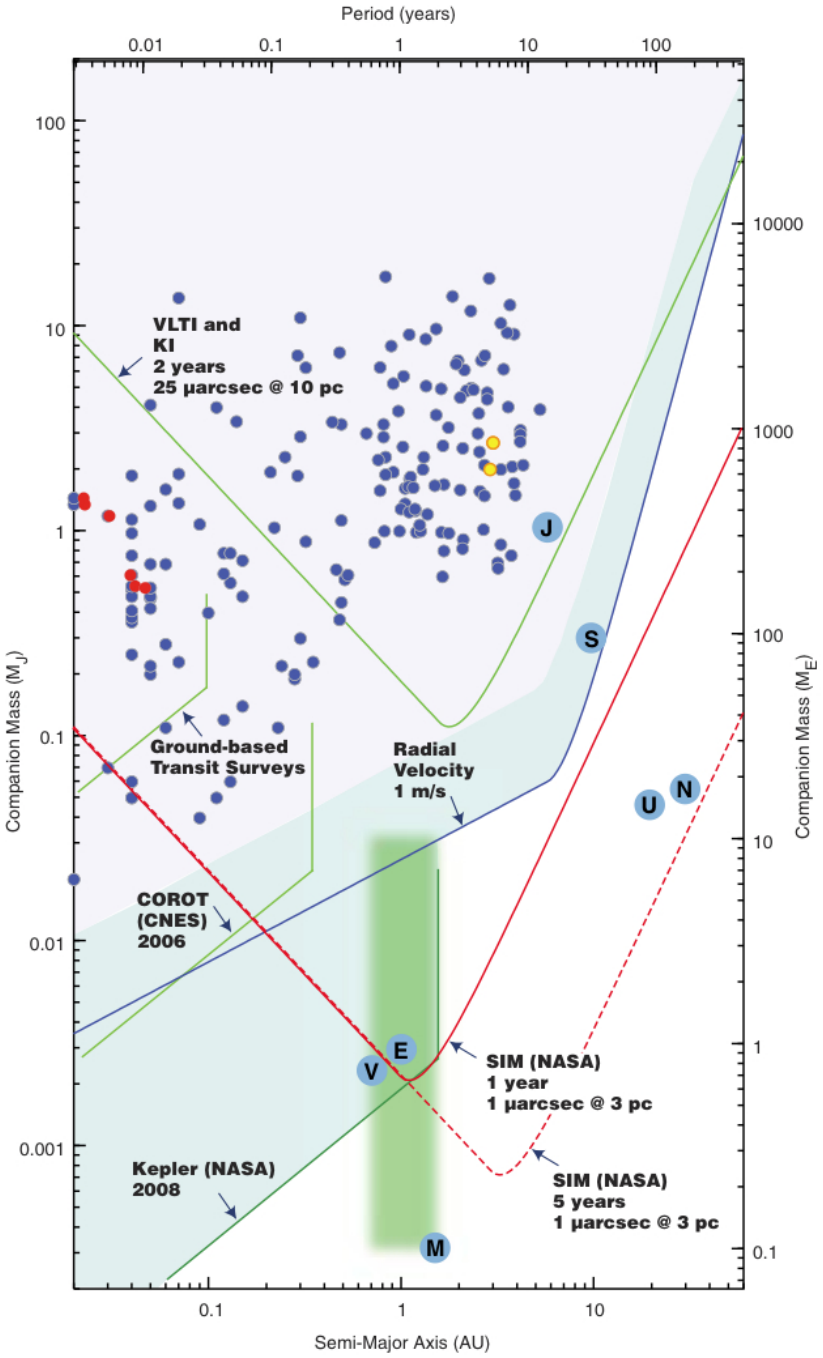

Figure 1.1 Limiting sensitivity of planet finding techniques. From Berriman et al. (2006). This shows the limiting masses and semi-major axes of the different techniques for finding exoplanets. Plotted are the planets of our solar system as well as known planets found with radial velocity studies (blue), transit studies (red), and microlensing studies (yellow). Not shown is the recent 5.5 Earth-mass planet discovered using microlensing surveys (Beaulieu et al. 2006).

using other methods to obtain more information. There is also the more practical problem presented as the environments created by the pulsar are not kind to life due to the intense electromagnetic radiation and creation event itself. This presents a tractability problem as exoplanets discovered from pulsar measurements usually cannot be studied via other methods and have a near-zero possibility for life. Because of their rare existence, the environment created, and small information that can be gained, pulsar measurements are not on the forefront of exoplanetary discoveries and analysis.

1.1.2 Radial Velocity Measurements From Doppler Shifting

The first discovery of an exoplanet around a Sun-like star came from radial velocity measurements (Mayor and Queloz 1995). Currently, the majority of accepted exoplanets have been found using radial velocity measurements. This method has also been used to confirm exoplanets discovered using a light curve analysis.

In radial velocity studies, a star's absorption features are measured as the star moves around the center of mass of the system. If there is no other object of sufficient mass in the system, the center of mass is near the center of the star - therefore no Doppler shift of the stellar absorption features are seen. However, if there is another object in the system, such as an exoplanet, then the center of mass is slightly different from the center of the star. As the star orbits around the center of mass, the Doppler shift in the stellar spectrum can be detected. The period of the orbit is related to the semi-major axis by Kepler's law and the amplitude is proportional to the projected mass of the companion along the inclination (M sin i). This is therefore a lower limit on the mass of the companion.

Doppler techniques rely on a massive planet orbiting the host star in order to detect the shifts in absorption features. As this has only been a recent method for discovering exoplanets (and the technique requires multiple orbits for confirmation), only short period orbiting exoplanets have been discovered. Exoplanets with longer period orbits have not had enough time to be discovered since this technique has been developed. For example, Jupiter would give a detectable Doppler shift to an

observer outside our solar system looking at our Sun, but it would take more than 11 years - the orbital period of Jupiter - to see this effect, and multiples of that for confirmation.

This technique is limited by the amount of "wobble" in the star's radial velocity, with current limits being as low as 1 m s^{-1} with ground-based observatories. This would be enough to barely see Saturn's affect on the solar absorption features (see figure 1.1). Another limiting factor is the ability to perform high-resolution spectroscopy on the host star in order to detect the Doppler shift. If the host star is too far and thus too dim to observe spectroscopically, then this method fails to work. Because this method is fairly easy to do yet gives relatively little information about the system, radial velocity studies usually take the form of surveys, with telescopes taking data over long periods of time, creating lists of potential exoplanets which are later analyzed. As more time passes and more surveys are carried out, an increasing number of exoplanets will be discovered with larger orbits.

1.1.3 Transit Studies Through Light Curve Analysis

When a planet transits its host star, there is an intensity drop in the light curve of the host star. This drop in intensity occurs when the planet eclipses the radiating star. By looking at the properties of the depth and width of the light curve, information can be gained about the orbiting planet, such as the radius of the planet. When information from the analysis of the light curve is combined with other methods, more can be found about the planet. For example, if the radius found through a light curve analysis is combined with the mass found from radial velocity measurements, the density of the planet can be found. The caveat in transit studies is that the transiting exoplanet must be aligned with the line of sight of the observer.

Properties of the system that can be learned through this method are similar to binary light curve studies. The radius, orbital period and inclination - from which, an actual mass can be determined - all can be found given the mass and radius of the host star.

In addition to observing the transit when the exoplanet is in front of the star, it is useful to observe the planet behind the star (called the secondary eclipse). The amount of radiation given off by the planet can be found by observing the drop in overall intensity of certain wavelengths (usually in infrared) during the secondary eclipse, which is usually much less than during the primary eclipse. This has been observed in HD 209458b in the infrared (Deming et al. 2005b).

Another advantage of transit studies is that if spectroscopic data are taken when the planet transits, one may be able to find features in the spectra from the exoplanetary atmosphere. In addition, if the depth of features are compared over the orbital period, the light curve of a feature is created. This feature light curve can determine the distribution of that molecule about the exoplanet atmosphere. This is an exciting, yet only recently explored, aspect of transit studies.

Future space observatories such as NASA's Kepler and Space Interferometry Mission (SIM) are planned to further expand the ability to find transiting exoplanets.

1.1.4 Microlensing

Gravitational microlensing was theorized by general relativity and was seen during total solar eclipses, but only recently seen elsewhere in the galaxy. The setup is shown in figure 1.2. An object passes in front of a background star, which is usually a great distance away. The light is bent around the object due to gravity and focused toward the observer (hence the "lensing" part of microlensing), thus increasing the overall intensity of the background object. A similar increase can be caused by a planet in the system of the initial lensing object. The advantage of using microlensing events to detect exoplanets is that it is sensitive to low mass planets. Figure 1.3 shows the lowest mass exoplanet discovered to date, a 5.5 Earth-mass planet. The event lasted just a few days and required many teams to collaborate to sample the entire light curve.

The disadvantage of the microlensing technique is that events are rare because they require precise alignment between the background object, passing object,

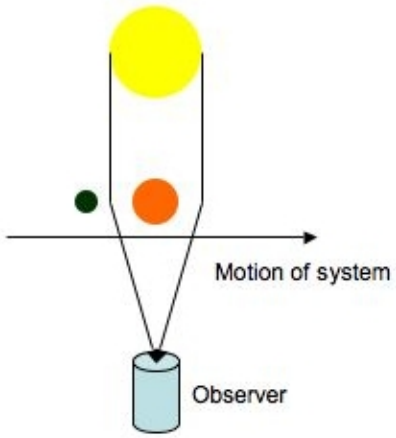

Figure 1.2 Setup of a microlensing system. The yellow object is the background star being observed. The orange circle is the microlensing object, and the green object is a potential planet producing another microlensing event. The light rays are bent around the object and focused towards the observer, producing an increased brightness.

and observer. Furthermore, these events only last for a short time (days to months). Finally, microlensing objects are not nearby, so spectroscopic followup is not feasible.

Recently microlensing surveys have used robotic telescopes to survey large areas of the sky to detect changes in the intensity of stars. These surveys often focus on the galactic center, so that there are a greater number of background stars and therefore a greater probability for a microlensing event to occur. When an intensity increase is observed, other astronomers are notified to perform more precise measurements of the intensity change.

Microlensing events are rare and non-repetitious, so they can only be used to discover exoplanets and determine only the mass. A worthy goal of microlensing surveys is to discover how rare or common exoplanets of a certain mass are. Despite the limitations, microlensing surveys have been given attention because they can discover low mass exoplanets.

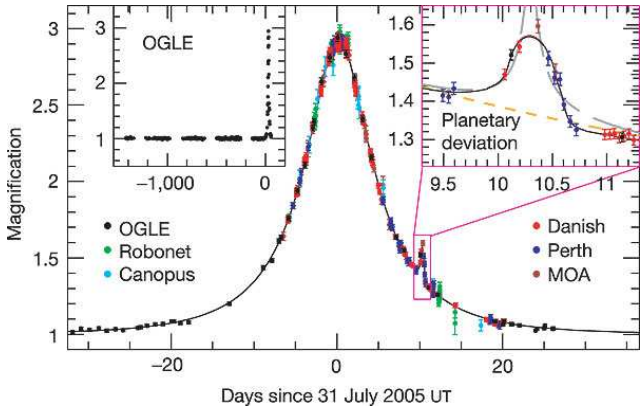

Figure 1.3 Adopted from Beaulieu et al. (2006). Shown is the light curve of the microlensing event. The large increase in intensity is due to the star passing between the observer and the background object, with the small increase at the end of the event due to the 5.5 $M_{\oplus}$ exoplanet.

1.1.5 Direct Observation

Many direct observations of exoplanets may not technically fall under their own categories, because some of the first direct observations have used methods previously mentioned. For example, two groups around the same time using the Spitzer Space Telescope detected infrared radiation coming from the exoplanets HD 209458b (Deming et al. 2005b) and TrES-1 (Charbonneau et al. 2005). They used the transit curve method studying the secondary eclipses of the respective host stars to find a decrease in infrared radiation coming from the system. This suggested that the exoplanet is contributing to the overall radiation of the system. Direct observation can take other forms through other methods, only requiring that the data come from the object itself to have the title of a direct observation.

Around the same time as the Spitzer discoveries, Hubble produced an image of an object around 2M1207 (Chauvin et al. 2004), which was assumed to be an exoplanet. This was later confirmed, with the planet having a huge radius, allowing it to be distinguishable from the host star in an image. Figure 1.4 shows an infrared image of the two distinguishable objects. While nearly impossible to view from

current ground-based telescopes, the next generation of space telescopes will hope to be able to make more direct observations of exoplanets similar to this image.

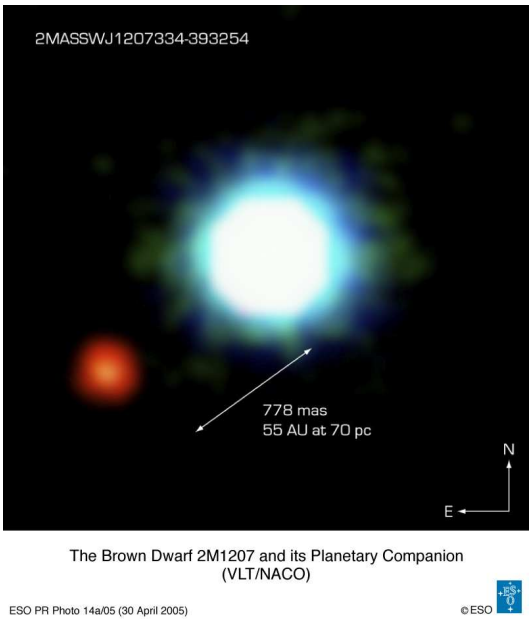

Figure 1.4 Adopted from Chauvin et al. (2004). This is an image of a direct observation of an exoplanet, with M= 5 ± 2 M_{Jup}.

1.1.5.1 Interferometry

Future missions such as the SIM and TPF will attempt to use the promising technology of interferometry to directly image exoplanets. Interferometry combines the images from multiple observations through constructive or destructive interference to enhance or "null" certain regions of an image. Interferometry has been used in astronomy for many years in radio observations, but only recently has become available in optical and near-infrared wavelengths with computers and more precise detectors.

This can be used to detect exoplanets by "nulling" out the host star. Usually the host star is too bright in an image to be able to detect an exoplanet, so by taking out (or significantly decreasing) the star's intensity in the images, previously unseen

objects become detectable. This process can also be used in spectroscopy, meaning future missions such as SIM and TPF will attempt to directly observe spectra of an exoplanet.

1.2 Scientific Motivation

One of the many ultimate goals of astrobiology is to detect a biomarker in an exoplanetary atmosphere. This would most likely take the form of the biomarkers mentioned earlier. However, because the study of exoplanetary atmospheres has only recently become feasible using high resolution spectroscopy and improved data reduction techniques, the first major steps have just been attempted toward this goal. While it is unlikely to be able to detect any of the biomarker molecules using current technology (because the contrast between the exoplanet and star is too great), it is possible to detect molecules with more reasonable features with larger column densities.

The limits on current technology are defined by the limits of data reduction and the limits of observations. For example, the size of space-based telescopes cannot improve without future missions. Observations on the ground have a greater chance to improve with more sophisticated and larger telescopes. However, even with constant improvement, the task of even detecting an atmosphere of an exoplanet is difficult. It has been suggested that the absorption features in the spectrum of an exoplanet would be $\sim 10^{-4}$ times weaker than that of the host star's intensity (Seager and Sasselov 2000). This requires high-resolution spectroscopy with very high signal-to-noise to make a detection. Currently, there have been no detection of particles in an exoplanetary atmosphere from ground-based telescopes. The only detections of atmospheric particles have come from the Hubble Space Telescope. Unfortunately, Hubble has no sensitivity in the near or mid-infrared where the contrast between the planet and star is favorable for molecular detections.

Understanding the atmospheres of exoplanets require advanced methods. The only examples of planetary atmospheres have come from studying the planets in our solar system. However, the exoplanet analogs to our own solar system, Jupiter

and Saturn, are much cooler than the majority of the exoplanets detected thus far. The models of hot Jupiters are not calibrated, and therefore are of unknown accuracy. It is unlikely that biomarkers will be detected on hot Jupiters, but detecting molecules from these planets is an important first step toward the more challenging observations of biomarkers from Earth-like analogues.

The initial steps in better understanding exoplanetary atmospheres can only be achieved through spectroscopically analyzing the exoplanet. This challenging observation has only been acquired through transit methods. This can be done through one of two methods. First, the host star is observed during the transit, and the spectroscopic data are compared to the spectrum out of transit (or that of a similar star to the host star). The difference between the in and out of transit spectra shows the spectrum of the exoplanet atmosphere. Second, the host star is also observed during the transit, but is not observed out of transit. This method occurs when searching for something that would not be native to the host star and therefore would not need canceling out. This can be done, for example, in molecular spectroscopy, where molecules would not occur in the host star due to the high irradiation in the photosphere that would destroy the molecule.

Because of the difficulty in detecting an atom or molecular absorption, searching at convenient wavelengths is a must. These advantageous areas of the electromagnetic spectrum are where there is a high probability or number of transitions as well as a (relatively) transparent area in the spectrum of Earth's atmosphere. Of course, if viewing from space telescopes, the Earth's atmosphere does not affect observations and therefore candidate particles to search for can be chosen purely by their abundance (and contrast ratio of star to planet).

H_3^+ is one such molecule, which resides in a relatively transparent part of the telluric spectrum. H_3^+ is created by the ionization of H_2, primarily through:

$$H_2^+ + H_2 \rightarrow H_3^+ + H \tag{1.1}$$

It has the strongest spectral lines where few other molecules have lines, making it easily distinguishable from other molecular transitions (McCall 2001). In Jupiter

and Saturn, H_3^+ has been detected in the ionosphere and has been attributed to ionization of H_2 by extreme ultraviolet electrons. A hot Jupiter - an exoplanet the size of Jupiter but with a much smaller semi-major axis - would be more ionized due to its proximity to the host star.

Detecting or placing a significant upper limit on the abundance of H_3^+ will demonstrate the technological feasibility of using ground-based telescopes to probe exoplanetary atmospheres. Additionally, H_3^+ is predicted to play an important role in regulating the thermal balance of an exoplanetary atmosphere (Yelle 2004), so observation of H_3^+ will provide an important test of this prediction.

The detection and analysis of H_3^+ can guide our models of the thermodynamics of the atmosphere because it is expected to be the dominant thermal regulator of the atmosphere. Finding the radial distribution of H_3^+ can be done through the comparison of the optical intensity versus orbital phase (a light curve) with the change in absorption of H_3^+ over orbital phase (an H_3^+ "absorption curve"). The optical light curve will give the planet's "classical" radius, and comparing absorption curve will show how H_3^+ is distributed about the exoplanetary atmosphere. If the absorption curve is wider than the light curve, then the "radius" of the H_3^+ in the planet is larger than the optical radius - H_3^+ is in the extended atmosphere, possibly escaping. If both curves are the same width, then H_3^+ is evenly distributed about the atmosphere. However, if the absorption curve is narrower than the light curve, this suggests that H_3^+ is located at specific areas of the planet. Because H_3^+ is created in regions where ionization of H_2 occurs, this would suggest that H_3^+ is being formed in abundance in regions where more energy is being deposited on the atmosphere. This is seen on Jupiter in the form of aurora. Therefore, if H_3^+ is detected and an absorption curve is created that suggests it is distributed locally, then it would show the presence of a magnetic field and exoplanetary aurorae. This would be a huge leap forward in exoplanetary studies, being the first detection of its kind.

The study of H_3^+ will advance the field for future studies by pushing current technology to its limit and highlighting potential improvements in the next generation of instrumentation. Furthermore, the successful observation of H_3^+ will

motivate the study of other atmospheric molecule using the techniques developed through this analysis. This project is an important step in determining the nature of exoplanetary atmospheres and fulfilling the goal of detecting a biomarker.

CHAPTER 2

HD 209458

2.1 Photometric Observations

2.1.1 Detection

HD 209458b was first detected in doppler surveys in 1999, which suggested a companion planet orbiting every 3.5 days. This was added to a list of candidate stars to search for a planetary transit. After times were calculated to find where the transit would occur, HD 209458 was observed photometrically, where it was shown that a planetary transit did occur (Henry et al. 2000). The inclination angle of the system was constrained, which, in turn, constrained the planetary mass and radius. For the first time, the parameters of a hot Jupiter were known precisely.

HD 209458 is a G0 star, with an effective temperature of 5942 K. It has approximately aged $\sim$4 Gyr (Melo et al. 2006), with a radius of 1.12 $R_{\odot}$, and is slightly metal-rich ([Fe/H]=0.04) (Fischer and Valenti 2005). These parameters place HD 209458 as a star somewhat similar to the Sun.

2.1.2 Basic Planet Parameters

Since the first discovered transit, the properties of HD 209458b have been calibrated and constrained even more. Some of these are shown in table 2.1.2 and displayed for comparison in figure 2.1. Most of the fits agree with the averages of the data, with the exception of the radius derived from Charbonneau et al. (2000). It should be noted that most of these parameters are dependent on stellar radius and mass, where a slightly different value for these will vary the planet parameters.

Taking a closer look at HD 209458b, Knutson et al. (2007) used stellar limb darkening models to predict the transit in different wavebands to determine the planetary radius at different wavelengths, which spanned around 0.01 R_{Jup}, which corresponds to about 700 km. This was a large enough difference to show up during the transit, as not all wavebands had the same light curve.

Radius (R_{Jup})	Mass (M_{Jup})	Reference
1.42 ± 0.10	0.62 ± 0.05	Henry et al. (2000)
1.27 ± 0.02	0.63 ± 0.05	Charbonneau et al. (2000)
1.40 ± 0.17	0.69 ± 0.05	Mazeh et al. (2000)
1.347 ± 0.060	0.69[a]	Brown et al. (2001)
1.355 ± 0.002	0.657 ± 0.006	Winn et al. (2005)
1.35 ± 0.07	0.66 ± 0.04	Wittenmyer et al. (2005)
1.320 ± 0.025	0.64 ± 0.06	Knutson et al. (2007)

Table 2.1 Comparison of the properties of HD209458b as given through different sources.
[a]This was derived from the given density, which was presented without error estimates.

2.2 Introduction to Transit Spectroscopy

Since discovery, HD 209458b has been under much scrutiny because it was the first transiting exoplanet discovered. Many of the parameters are well constrained, making it easier to model the atmosphere and build upon previous results. As mentioned earlier, transiting exoplanets give an unprecedented view into the planetary atmosphere, as the features can be potentially seen in both emission and absorption while it transits and travels around the host star.

Despite being the size of Jupiter and transiting every few days, these observations are very difficult to make from the ground, and have only been successful in detecting the exoplanet atmosphere from space-based telescopes. This is because the column density of molecules in the line of sight to the star needs to be very large, mostly due to the limited optically thin area of the planetary atmosphere.

Absorption features can be detected as the light from the host star, which is now providing the background radiation, gets absorbed as it passes through the atmosphere to our line of sight. The atmosphere needs to have a large column density of material in order to absorb the radiation. The most likely absorbers are going to be things found in the atmosphere of the host star as well, as the temperatures for hot Jupiters are on the order of the host's temperature. However, because they

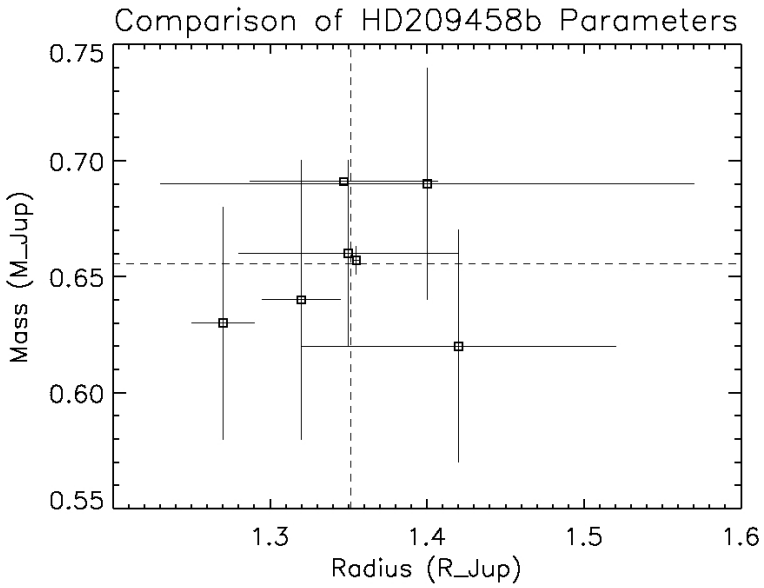

Figure 2.1 This is a graphic representation for the derived radii and masses from different sources. The error bars are shown as well, with the averages of both the radii and masses as the dotted line. They meet very near the data presented in Winn et al. (2005) and Wittenmyer et al. (2005).

are not as hot as the atmosphere of the star, they can have some molecules with a higher dissociation threshold.

Detecting features in emission could occur in and out of the transit and could come either from the planet or elsewhere. Because of the intense irradiation from the host star, the atmosphere could be escaping. In fact, this is seen in hydrogen in the atmosphere of HD 209458b (Vidal-Madjar et al. 2003), where it is observed beyond the Roche lobe. This is similar to a comet as it travels near the Sun, where the comet's outer material will heat up and leave a tail. This material can remain in the planet's orbit, but not necessarily be physically located with the planet. A cloud of material could form around the host star, which is constantly receiving radiation from the host star. This would be re-radiated toward our line of sight, which would be seen in emission.

As mentioned, the emission can also occur at the exoplanet while it transits. While it is true that most hot Jupiters are tidally locked, the planet may still have weather patterns on the surface. These systems could transport the heat to the dark side of the planet, where it is optically thick, meaning emission to our line of sight during the transit. The emission could also be from objects that would not survive on the bright side of the planet, but would on the cooler "dark" side. When detection techniques improve, this could provide an opportunity to look for molecules that would be good tracers of the weather patterns in the atmosphere of the planet.

What is the balance between the possible emission and absorption mechanisms? The answer to this question is very important to the ability to observe the atmosphere of an exoplanet. This thesis attempts to detect a molecule in the atmosphere of the exoplanet, which will describe the interplay between the stellar flux and the thermosphere of the exoplanet.

2.3 Spectroscopic Models

Modeling of exoplanet atmospheres is the best way to guide future observations, and can be used to study re-radiation, temperature-pressure atmospheric profiles, theoretical transmission spectra, and many other ideas.

Modeling of exoplanet atmospheres involves many components, the most important of which is the chemistry. The chemistry of an exoplanet remains somewhat uncertain as most models use solar abundances of elements, despite the fact that some elemental abundances may not be solar, specifically oxygen and carbon. Higher metal abundances can occur when metal-rich planets accrete onto the host star. The extreme ultraviolet radiation will irradiate the atmospheric hydrogen, producing an escaping atmosphere. However, the escaping atmosphere, even though large, will not be a large fraction of the total planetary mass. The most important absorbers (and therefore those detectable in an atmospheric spectrum) are H_2O, CH_4, NH_3, Na, and K (Marley et al. 2007).

Another important factor to guide observations is the effect of clouds and dust grains in the atmosphere of the exoplanet. Atmospheres with clouds would scatter photons (and increase optical depths at different wavelengths) before they get deep into the atmosphere, leading to a higher overall reflectivity in the red and near-infrared. Modeling clouds and particles are typically one-dimentional, despite the fact that it is intrinsically a three-dimensional problem.

In a direct example of modeling, Seager and Sasselov (2000) create models of close-in extrasolar giant planets and estimate transmission spectra. The goal of these models are to determine where clouds exist in the atmosphere, and therefore the most advantageous wavelengths at which to observe.

Added to the problem with clouds and particles, vertical mixing and atmospheric dynamics are other difficult modeling complications. Vertical transport is especially important if the dynamic timescales are short to the chemical equilibrium timescales. This causes chemical discrepencies at different planetary radii depending on temperatures, most likely causing a unique spectrum for each hot Jupiter.

The models puts a huge constraint on the atmospheric transmittance based on the radii of the cloud tops. The models show in general that the absorption features (of which the main constituents are H_2, CO, H_2O, and He) will be apparent over the stellar background, but will be a factor of 10^{-4} less intense than that of the stellar background. Many of the predictions made by their models can be constrained by observations. For example, observing the change in the light curve over time during first part of the transit with high enough accuracy could give the temperature and column density for different heights in the exoplanetary atmosphere. Also, detection of alkali metals would confirm a postulate that the atmospheres of these planets are similar to cool dwarfs and have similar temperatures.

Models have been checked by successfully predicting the atmospheres of the giant planets in our solar system. Two such examples that directly impact the motivation for this thesis are Miller et al. (2000) and Yelle (2004), who use models to predict the column density of H_3^+. Miller et al., motivated by H_3^+ in Jupiter, used an accurate atmospheric model of Jupiter to change the distance from the host star from

5 AU to 0.05 AU. They predict a column density of 10^{14} cm^{-2}, which they describe as an underestimate because it does not allow for the atmospheric expansion. Yelle used one-dimensional models to predict equivalent widths for different molecules, suggesting that the highly active H_3^+ molecule will be important in the thermal regulation of the atmosphere, which is usually not included in other models. The Yelle models do not predict as large an amount of detectable H_3^+ as Miller et al. did, but do not describe whether their value makes it possible to detect from ground-based telescopes.

One final complication comes from the stellar radiation, which may produce non-LTE effects that have yet been unconfronted. The non-LTE could produce population levels different from that currently used in LTE atmospheric models. Some newer models have used 3-D modeling to show there might be tidal atmospheric currents from the dayside/nightside heating and cooling.

2.4 Spectroscopic Observations

2.4.1 Unsuccessful Attempts

There have been many unsuccessful attempts to detect the atmosphere of HD 209458b, perhaps due to unknown difficulty and complications. For example, unrealistic integration times because of the transit schedule create near-impossible situations to analyze regular data, let alone those where an absorption feature will be much less than 1% of the continuum (Moutou et al. 2001).

An interesting non-detection is that of Deming et al. (2005a), who had a large amount of observing time using NIRSPEC of Keck II. Models that correctly predicted a detectable sodium absorption (mentioned in the next section) in the atmosphere of HD 209458b also predict a detectable absorption of CO. However, there was no detection of CO. To check their methods, the predicted spectrum of the planet (which was correct, but predicted a higher amount for sodium) was input into their data analysis, which returned the predicted absorption, meaning the data technique was correct. The non-detection adds to questions, as some theories

explaining the low detection of sodium do not account for the low (zero) absorption of carbon monoxide.

There are a few possibilities for the non-detection of CO. First, there could be a large temperature gradient from the side facing the host star and the side facing away from the host star. This would decrease the mixing of the CO in the atmosphere of the cooler side, which would show lower overall absorption. Another possibility is there are high clouds causing higher opacity or a decreased temperature in the upper atmosphere of the exoplanet.

A model with high cloud tops correctly fit the data of both Charbonneau et al. (2002) and Deming et al. (2005a). Deming suggests that either clouds at observable wavelengths exist or the temperature of the planet is cooler than previously assumed.

2.4.2 Successful Detections

In 2003, (Charbonneau et al. 2002) used the STIS spectrograph on the Hubble Space Telescope to study HD 209458. A sodium absorption feature at the 589.3 nm resonance doublet was discovered by comparing the in-transit spectrum of the host star with the out-of-transit spectrum. The absorption feature is only deeper by a factor of $\sim 10^{-4}$ compared to the out-of-transit spectrum, despite the prediction of a depth of $\leq 0.1\%$. This was not matched in their observations due to some other factors, including cloud cover of the planet or an overall lower abundance of sodium than previously expected. The latter is unlikely as the predictions for sodium were based off of the host star's metallicity, which should be very close to the metallicity of the planet.

Atomic hydrogen has been found in the hydrodynamically escaping atmosphere of HD 209458b (Vidal-Madjar et al. 2003). The amount of escaping material is not be large enough to make hot Jupiters short lived. However, it could cause hot Jupiters to become Neptune-mass planets that are hydrogen poor. Vidal-Madjar et al. (2003) suggest this could be why there have been a dearth of planets detected with orbital periods less than 3 days.

Following the previous discovery of Sodium and escaping Hydrogen, Vidal-Madjar et al. (2004) followed up their previous work by using the STIS spectrograph on Hubble, finding oxygen, carbon, and hydrogen in the atmosphere of the exoplanet. In the wavelength range in which they were observing was also nitrogen, silicon, and sodium. These molecules had no feature that were detectable using their methods. By comparing the in-transit and out-of-transit flux, they show that there is an appreciable difference in flux for hydrogen, oxygen, and carbon.

Because the amount of absorption for an object is related to the how the object is distributed around the exoplanet, the ratio R_{abs}/R_* can be found from the amount of absorption. Different percentages of absorption represent different radial distributions of the particle. Using this argument, nearly all three are extended out to the Roche lobe, with Hydrogen exceeding it - and thus the "escaping" atmosphere.

2.5 Other Transiting Exoplanets

2.5.1 HD 149026b

This planet has a smaller radius than HD 209458b with a mass of $M = 0.35 \pm 0.03\ M_J$ and a radius of $R = 0.0725 \pm 0.05\ R_J$ (Fortney et al. 2006). Previous analysis of solar metallicity hot Jupiters would suggest that smaller mass planets would be larger from the influence of radiation from the host star. Because HD 149026b is smaller than what would be predicted, there may be a larger amount of heavy elements in the interior of the planet with a large massive core. This would be entirely different from other Pegasi planets (such as HD 209458b). Much is known about gas giants such as Jupter and Saturn, but comparatively little is known about ice giants, which is what HD 149026b could be. The difference between ice giants and gas giants is the metallicity in the interior of the planet, which may be different than the metallicity of the host star. HD 149026 has a higher metallicity than HD 209458, which may suggest a higher probability of creating an ice giant.

One of the future goals of this project is similar to what was done by Shkolnik et al. (2006). Shkolnik et al. observed six sources for H_3^+ features, but could find no detection. They place upper limits on the column density of H_3^+, which is

unfortunately higher than the prediction of both Yelle and Miller et al. This study is important because it shows the difficulty in detecting a molecule from ground-based telescopes.

CHAPTER 3

THE H_3^+ MOLECULE

In order to better understand why this project focuses on H_3^+, a better understanding of this molecule is necessary.

H_3^+, a triatomic molecule created in environments of ionized molecular hydrogen, is created primarily through:

$$H_2^+ + H_2 \rightarrow H_3^+ + H$$

There are no bound electronic transitions, so any such transition destroys the molecule. This occurs at 4.5 eV or, in terms of temperature for thermal destruction, at around 2500 K. No pure rotational states occur, because no permanent dipole exists due to the symmetry of the molecule. The only observable transitions are ro-vibrational transitions, the strongest existing in the near-infrared.

Because H_2 is the most abundant molecule in the atmosphere, one might ask why that is not the subject of observation. Unfortunately, H_2 is difficult to detect, because of the weak oscillator strengths of the ro-vibrational transitions.

3.1 H_3^+ Importance

H_3^+ is created in regions where molecular hydrogen is photoionized. It has been detected in molecular clouds (McCall et al. 1999; Melin et al. 2005; Goto et al. 2002), and has also been detected in the outer planets of our solar system - in Jupiter (Broadfoot et al. 1979; Miller et al. 2000), Saturn (Geballe et al. 1992), and Uranus (Trafton et al. 1993). H_3^+ has been detected in Jupiter's ionosphere, it would be expected to be in the atmosphere of a hot Jupiter as well, where the ionizing UV radiation will be stronger.

H_3^+ is advantageous because the strongest spectral features occur where few other molecules have lines, making it easier to analyze. For this project, the R(1,0) and R(1,1)^u states will be observed, which are two fundamental transitions that are

observable in the same spectral grasp. The molecular spectroscopic notation is as follows:

$$\{R, P, Q\}(J, K)^{(u/l)} \tag{3.1}$$

where the letter in front represents the J transition J+1, J+0, or J-1 for R, P, or Q respectively. The letters J and K represent the rotational quantum numbers. The letter u or l represents the upper and lower transition for the degenerate para state. For example, the R(1,1)^u transition is the fundamental transition from J=1, K=1 rotational quantum numbers to the upper J=2, K=1 quantum numbers. The specific wavenumbers of the states are in table 3.1.

Existing in environments where there are incoming ionizing photons, H_3^+ is dominant in the thermal balance of the planetary ionosphere. Studying H_3^+ gives important information about the planetary atmosphere. For example, if H_3^+ is detected above predicted amounts, it may suggest that H_3^+ is escaping from the atmosphere, similar to the escaping atomic hydrogen (Vidal-Madjar and Etangs 2004).

Similarly, if there is no detectible H_3^+ in the atmosphere, it may suggest that H_3^+ is being mixed to a deep level of the atmosphere, which destroys the molecule. It could also mean that H_2 is not present in the upper atmosphere, possibly because it is being dissociated to a deep level, where the column densities are such that H_3^+ is undetectable.

Transition	Wavenumber (cm^{-1})	Wavelength (μm)
R(1,0)	2725.885	3.6685
R(1,1)	2726.208	3.6809

Table 3.1 Table of transitions of the H_3^+ molecule that were measured for this thesis.

Information about silicate cloud tops can also be gained from atmospheric observations. The cloud tops and depths depend on the heating of the atmosphere and thermal balance, which is dependent on the properties of the grains in the upper

atmosphere. Seager and Sasselov (2000) suggest that cloud tops affect the ability to detect molecules in the atmospheres of exoplanets, as the silicate clouds scatter light and provide a greater optical thickness to the atmosphere. If the atmosphere is optically thick higher in the atmosphere, then an absorption feature will be harder to detect.

3.2 Previous Observations of H_3^+

This section will discuss other observations or attempted observations of H_3^+ in the scientific community. Attempts have been made to observe H_3^+ in the atmospheres of other exoplanets, but have thus far been unsuccessful. Observations of H_3^+ have been successful in atmospheres of much closer planets - namely Jupiter and Saturn. H_3^+ has also been observed in the ISM, which will be discussed below.

3.2.1 H_3^+ in Other Exoplanets

There have been attempts to detect H_3^+ in the atmospheres of other exoplanets. Perhaps the most notable of these studies is from Shkolnik et al. (2006). In this study, five exoplanets were observed during their transits, one of which was not HD 209458b. The attempt was to compare to both the predictions of Miller et al. (2000) and Yelle (2004). The observations were done on the Q(1,0) transition, which is slightly different from the ones observed in this thesis. One transit was observed for all of the exoplanets, but unfortunately upper limits were not lower than those of the predictions. In fact, one upper limit was above that achieved in this thesis (see chapter 4). This study is important for many reasons. First, it shows the community interest in this research in the form of a journal publication. Second, it shows that the results obtained for this thesis are on track with others in the community. Finally, Shkolnik et al. (2006) suggest that with another transit observation, a quantifiable signal may be detected.

3.2.2 H_3^+ in the Outer Planets

The idea to search for H_3^+ in the atmospheres of exoplanets came from a well characterized system much closer to Earth - namely, Jupiter. H_3^+ has primarily been

seen in the aurora of Jupiter. Electrons from the solar wind are collimated down the magnetic field lines of Jupiter to collide into the ionosphere near the poles. The electrons ionize a region of molecular hydrogen, producing aurora similar to what we observe on Earth. This energy deposition can ionize H_2, which provides the needed environment to create H_3^+. A measured H_3^+ spectrum is seen in figure 3.1 (From Miller et al. 1990).

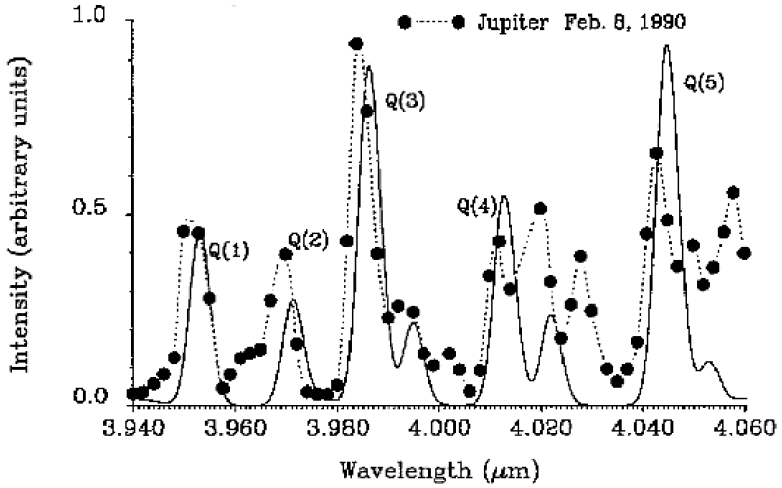

Figure 3.1 H_3^+ is seen in the atmosphere of Jupiter, primarily in the polar, auroral regions. From Miller et al. (1990). In the atmosphere of a "hot Jupiter", the strongest features will not be the same as here, due to different stellar irradiation.

CHAPTER 4

DATA

The data analyzed in this thesis were acquired with PHOENIX on Gemini South on September 6th, 2005. PHOENIX is a near-infrared high-resolution spectrometer with resolution between 40,000 and 75,000, depending on the slit width. For this observation, a resolution of ∼45,000 was used. There were 40 sets of exposures taken over the course of 5 hours, 20 minutes, using an ABBA pattern. This is a technique used to remove sky components, where 4 exposures are taken with the star in 2 different positions - an A and B position. The first A exposure is taken, then the star is "nodded" to a different position along the spectrograph slit, to create the B exposure. The second B exposure is taken in the same position, after which the star is nodded back to the original position for the final A exposure. An ABBA frame consitsts of $(A_1\text{-}B_1\text{-}B_2\text{+}A_2)/2.0$, and is shown in appendix A.

The time of observation was chosen to coincide with a transit of the planet HD 209458b across its host star. This would allow the upper atmosphere of the exoplanet to be irradiated in the line of sight with the host star, so that H_3^+ will be observed in absorption. Data were gathered from 1 hour and 40 minutes before the center of the transit to 3 hours after.

4.1 Data and Models

The reduction algorithms used are described in Brittain (2004), however a brief description of some of the specific algorithms used are described in Appendix A. The algorithm converts raw data files created during observation into arrays of spectra. These spectra are then compared to (Earth's) atmospheric models created by a separate program. The Spectral Synthesis Program (Kunde and Maguire 1974), which accesses the molecular transitions from the HITRAN-1996 database (Rothman et al. 1998). The model is ratioed with the data in order to correct for wavelength-dependent transmittance of the atmosphere.

A sample single frame is shown in figure 4.1. The two H_3^+ features reside within telluric features. The width of the lines shown in the figure is the Doppler shift of the H_3^+ features throughout the night's observation. The telluric features dominate the shape of the spectrum and need to be removed to get out the useful science information.

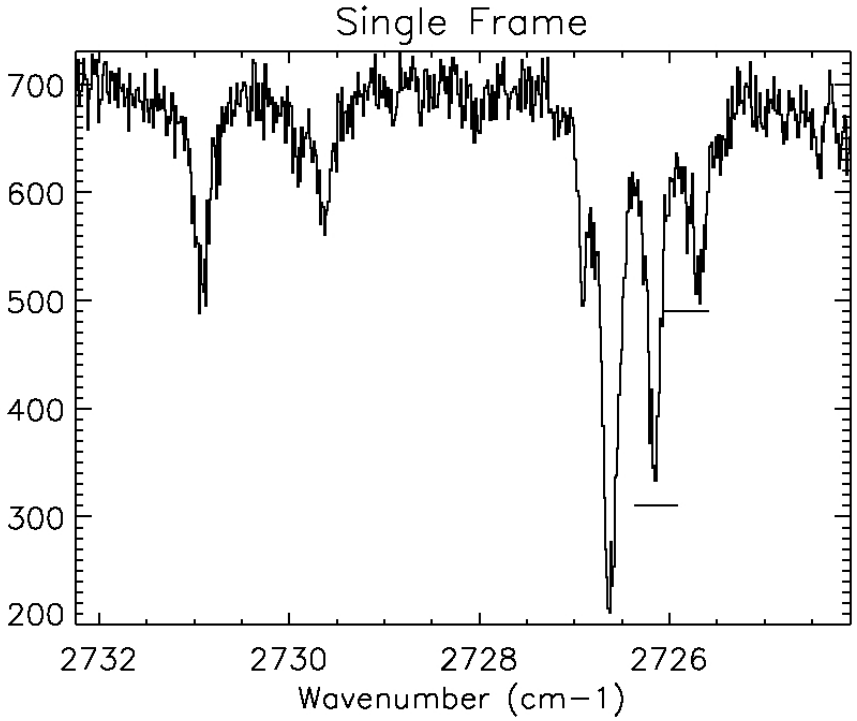

Figure 4.1 A single spectrum shown, with the H_3^+ features shown as the solid horizontal line. The width of the lines is the range of the Doppler shift due to the planet orbiting around the host star. As it can be seen, the features lie within telluric features, making it more difficult to make a detection.

The telluric model is created by the SSP model mentioned earlier. The output model is shown in figure 4.2. The SSP model was calibrated for the telluric spectrum above Mauna Kea in Hawai'i (altitude of 13,679 ft), and therefore had to be altered for the atmosphere above Gemini South in Chile (altitude 8,930 ft). The higher altitude of Mauna Kea results in a lower column density of

water to look through while observing. This was changed by altering the input files in the SSP program to account for higher perceptible water. Also, information about temperature, humidity, etc. was gathered from the weather station archive (http://www.ctio.noao.edu/environ.html). Similarly, the model allows for the amount of certain molecules to be altered. Using mixing ratios from Van-Loon (2000), the specific amount of molecules were tuned to be more accurate for the southern hemisphere. These alterations can be justified because they have accurately predicted the telluric spectrum for Mauna Kea using real physical data. Changing the input to the SSP model to more accurately reflect the environment around Gemini South should give an accurate telluric spectrum. Similarly, the main features in the spectrum come from the Earth's atmosphere, so cavalier alterations to these features have obvious repercussions. For example, the main feature at $\sim$2726.6 cm^{-1} is due to CH_4. If the CH_4 is changed a small amount, the depth of this line will not match up with the raw data, making an inaccurate comparison.

4.2 Reduction

For each ABBA set, the resulting raw spectrum was "fit" with a telluric model. Fitting refers to creating a wavenumber calibrated spectrum by matching the telluric features in the model with the features in the data. Each model was calibrated individually because of the changing weather over the course of the night. The temperature slowly dropped over the course of the night, while the humidity and barometric pressure fluctuated slowly. Likewise, if a cloud passed overhead, there wass a noticeable difference in the H_2O features. Each of these variables had to be accounted for by slightly altering inputs to the telluric model.

Dividing the raw spectrum by the model gives a ratioed spectrum, which can be used to extract the scientific information. This is equivalent to looking at the spectrum of the star, as the telluric features have been removed. In this part of the spectrum, the absorption and emission from components of the host star are very minimal, especially around the H_3^+ features. This means that if a feature exists

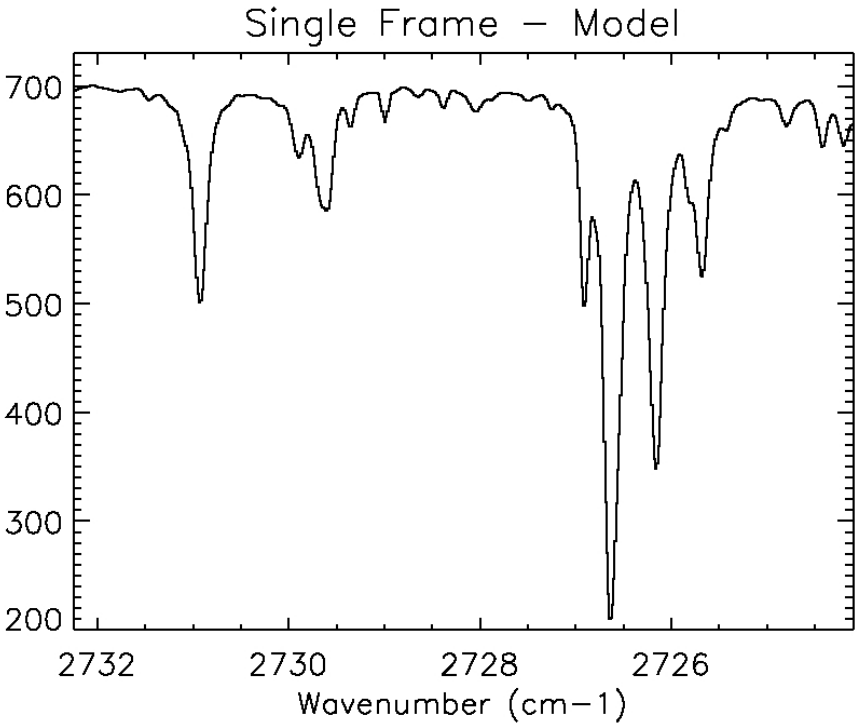

Figure 4.2 A single model telluric spectrum shown, created by the SSP program. The main molecules that dominate the spectrum are CH_4 and H_2O.

at the expected location, it will be due to H_3^+ and not from a component of the host star.

The ratios of all forty ABBA set are shown in figure 4.3. Each ratio is just the raw spectrum divided by the model for that set. In some cases, the fit is not perfect, and produces a false feature. These large features are easy to spot and easy to fix. When a feature is deep, the photons from the star are being absorbed, which gives no useful information about the star (or exoplanet). Because of this, areas where low transmittance occurs are singled out, and the ratio of those areas are set to unity. For the purposes of this thesis, the threshold of transmittance was set to 70%. This high threshold is set as such because of the accuracy needed to find the H_3^+ feature, which is expected to appear at $\sim$0.05%.

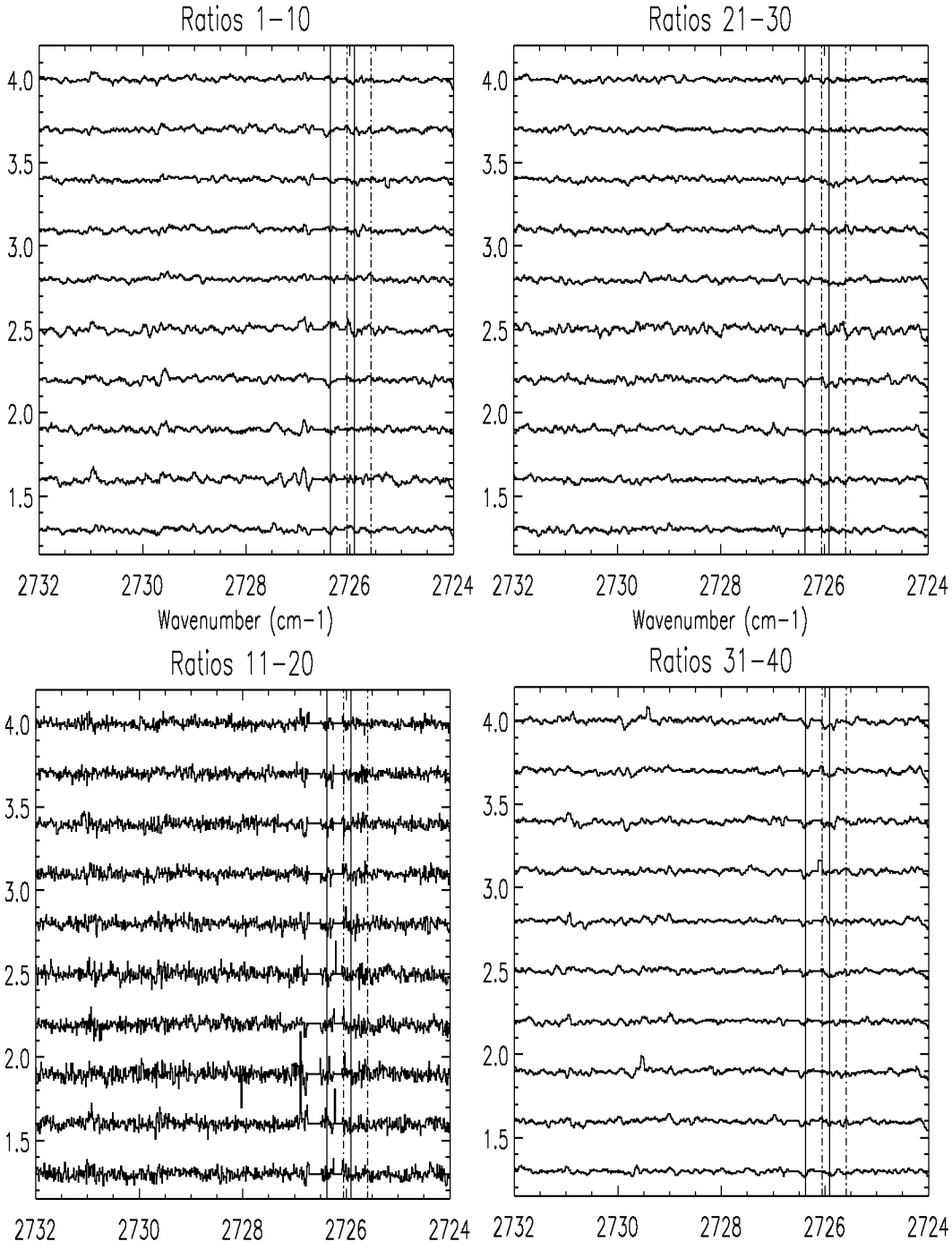

Figure 4.3 Shown are the ratios for every ABBA set offset for clarity. This is plotted just to show that overall, the fits are good. The solid vertical lines is the Doppler shifted area for the R(1,1) feature and the dot-dashed vertical lines are for the $R(1,0)^u$ feature.

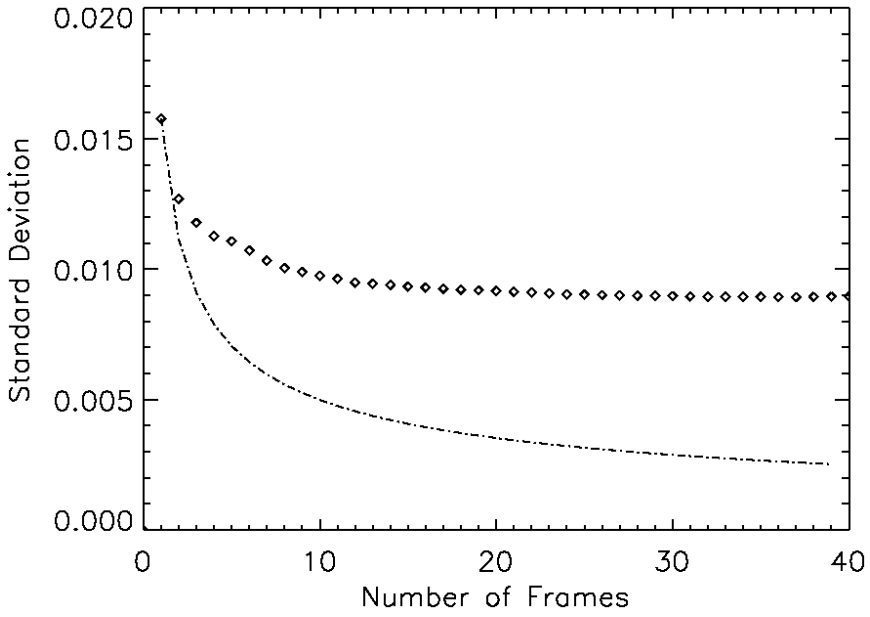

Figure 4.4 This shows the decrease in the standard deviation of the mean over time when adding more frames. The dot-dashed line is the theoretical line of $1/\sqrt{N}$. After only about 14 frames, the standard deviation does not decrease as much as the theoretical line. This is mostly because of systematic errors and fringing that will be removed and discussed later.

Adding frames together should decrease the random noise that exists in the spectrum. Ideally, the error in the mean of the data, which will be referred to as the standard deviation, should decrease as $1/\sqrt{N}$. For example, adding four frames together should halve the standard deviation of the mean. In practice, though, this is not achieved. As seen in figure 4.4, the standard deviation falls above the theoretical $\sqrt{N}$, mostly because of systematic fringes. These fringes are intrinsic to the spectrum, so canceling out the random noise does not cancel out the fringes. This means that more observations and integration time will not further decrease the standard deviation.

The ratios that have been created can now be manipulated to search for the H_3^+ feature. The reduction process is not just as simple as averaging the entire set. Each individual ratio is from a specific time in the orbit of the exoplanet. As the

planet orbits, the H_3^+ feature is Doppler shifted. This shift is small (∼8 pixels), but still requires correction. The shifted ratios can then be summed to produce a final spectrum, from which a feature or an upper limit can be observed. Appendix B uses a simulated set of data to illustrate the need for the shift.

4.2.1 Unshifted Ratio

For use in a direct comparison with Appendix B, the same steps will be compared for completeness. The average ratio is calculated using two steps. First, the sections of each ratio that fall below the transmittance threshold were marked. Thus, for each pixel, there was a weight of useable pixels that can be used (where the transmittance is above the threshold). Then the average ratio was calculated using the weighting factor, set to unity where the weighting factor is less than five. The reason for choosing five was aesthetic, but it seemed that when there were less than five good pixels, it meant that the pixel was on the wing of a telluric feature, and was not always a good model fit.

Figure 4.5 shows the average unshifted ratios (shown closer in figure 4.6). Notice that there is no three-sigma detection. Therefore, more must be done in order to decrease the standard deviation. As shifting does not decrease noise, this process should not improve the the signal-to-noise.

4.2.2 Shifted Ratio

As described in Appendix B, the ratios need to be shifted to account for the Doppler shift of the expected feature, due to the orbit of the exoplanet. To do this, the shifts need to be calculated. First, the maximum velocity needs to be calculated. Using the simple relation of orbital period and semi-major axis, the maximum velocity can be found,

$$V_{max} = \frac{2\pi R}{P} \tag{4.1}$$

where R is the semi-major axis (0.045 AU) and P is the orbital period (3.524 days). This leads to the max velocity of 138 km s^{-1}. From this, the velocity at any point

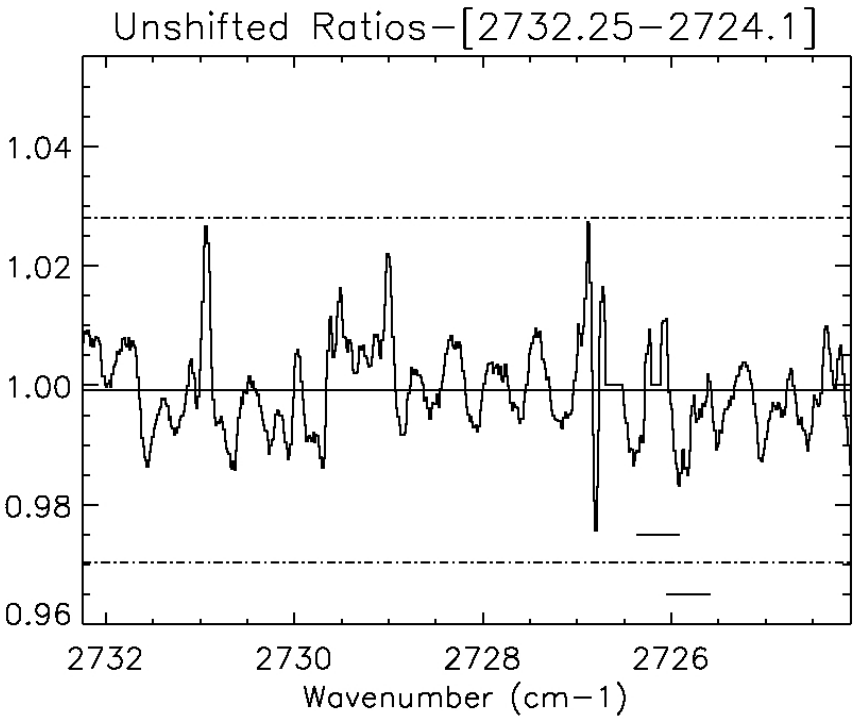

Figure 4.5 Plot showing the average of the unshifted ratios. There does not appear a noticeable feature around the two H_3^+ ranges, at least not above a three-sigma value, which is shown by the dot-dashed line. The solid line is the average. Both are shown over the range for which each was calculated.

can be found by determining the orbital phase. The orbital phase is just the time of observation mod the orbital period. The orbital phase can be plugged in to find the velocity as follows:

$$V = V_{max} sin\left(\frac{t - t_c}{P}\right) \tag{4.2}$$

where t_c is the time of the central transit and P is the period. The velocity can be finally used in the doppler equation to find the shift in wavelength (wavenumber) over the period of observation. For each frame, the velocity was calculated by using the UT time in the header of the first B-frame in the ABBA set. This provided an accurate measure for the time of observation in relation to the transit time. This also gives an accurate measure of the Doppler shift in the feature.

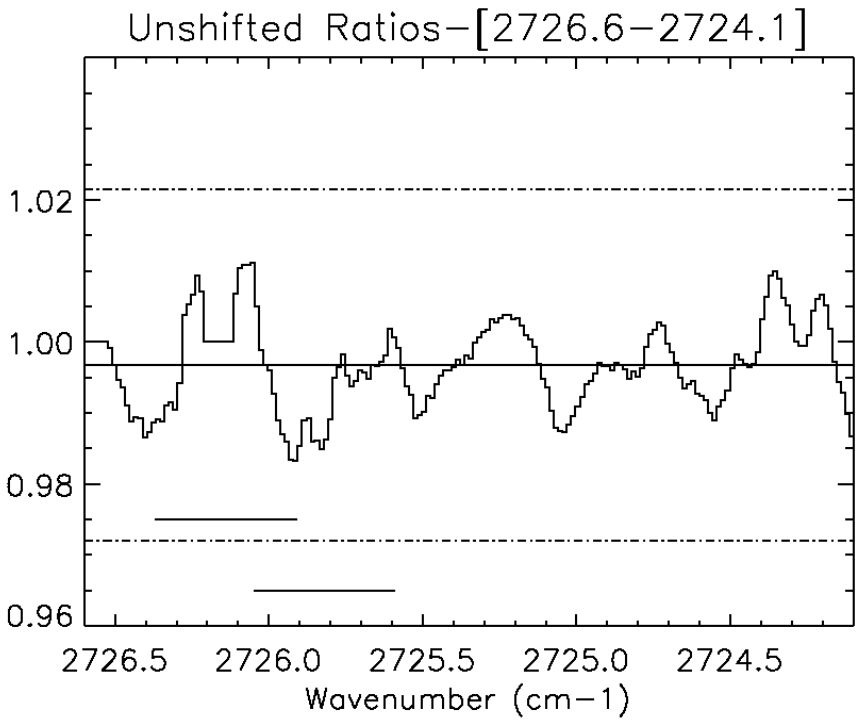

Figure 4.6 A closer view of the unshifted ratio.

There is one final velocity correction that was made, which does nothing to alter the true data, but rather to shift the central velocity. The motion of the star relative to the solar system, otherwise known as the heliocentric velocity, should be accounted for. The motion of the star relative to the Sun is -14.8 km s^{-1} (Montes et al. 2001). This just shifts the central velocity, or shifts the data in figure 4.8 to the left or right.

For this reduction, the spectra were converted into velocity space. The velocity of zero was set to be the central wavenumber of the shifted R(1,0) feature. The velocities of other pixels were found by interpolating the velocity needed to shift to the central wavenumber. Each frame was then binned in velocity space, which is shown in figure 4.7, and closer in figure 4.8. The range from ∼-500 km s^{-1} and lower is flat because that part of the chip was not reliable. This does not affect the

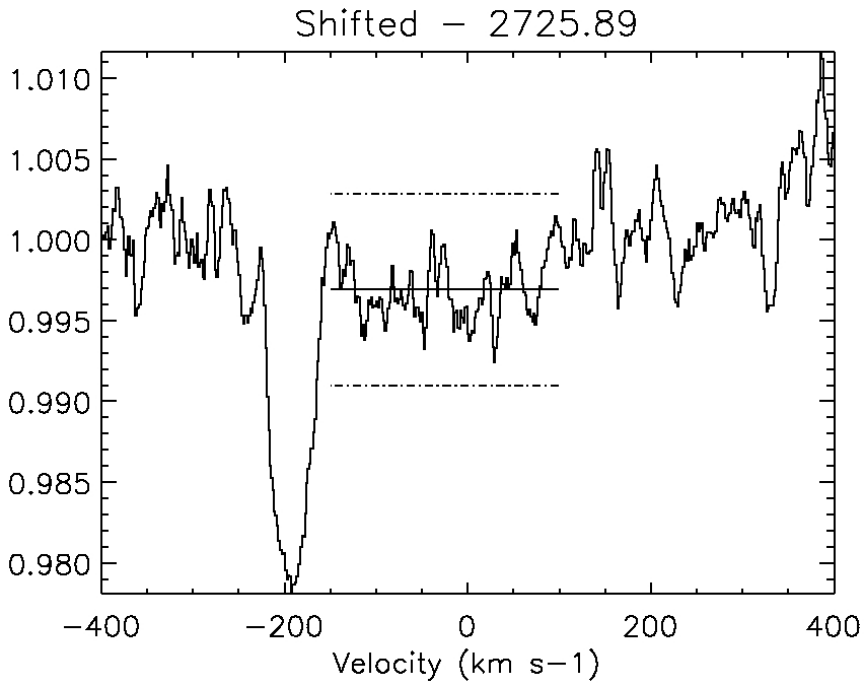

Figure 4.7 Plot of the shifted and averaged ratio. Still, a three-sigma detection cannot be made. However, we now have a much lower upper-limit that can be made. The dot-dashed line is the three-sigma level, while the solid line is the average. Notice that the three-sigma level has been reduced significantly. Again, the range over which the limits and average are plotted is the range over which they were calculated.

overall science, as that part was not used to calculate the standard deviation and did not fall around the zero velocity.

4.3 Fourier Analysis

In figure 4.7, there seems to be a systematic, or periodic, fluctuation in the ratio. This is due to a fringing pattern coming from internal reflections in the instrument, which is not part of the science spectrum. Also, as the telescope tracks the star across the sky, the grating can slip slightly, which introduces similar patterns. These systematic components can be removed by finding spikes in the power

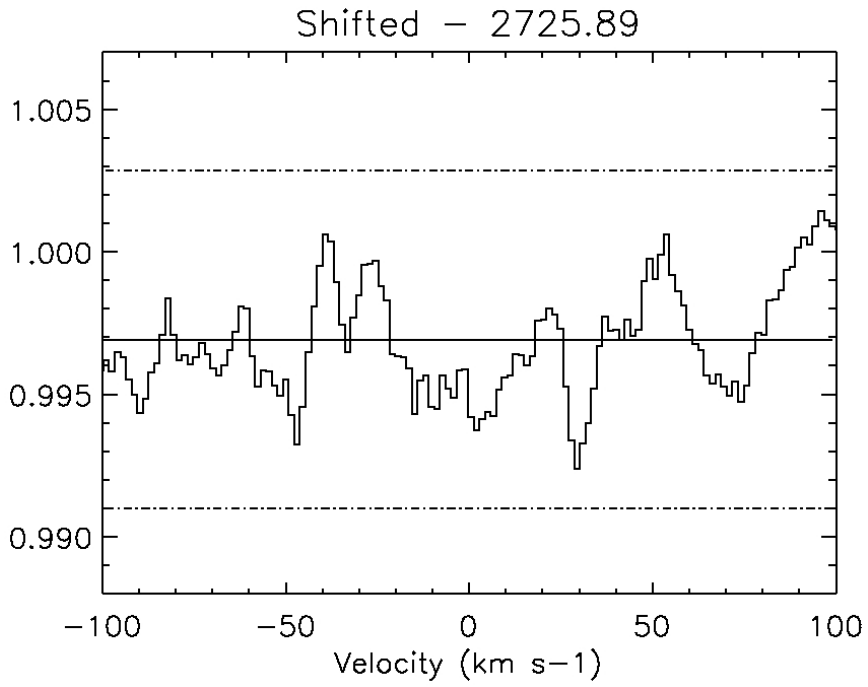

Figure 4.8 A closer view of the shifted average ratio. The three-sigma level is around 0.5%. Note: the range over which the average and three-sigma level were calculated extends beyond the view plotted here.

spectrum. Once these components are removed, the science part of the spectrum becomes clearer.

The Fourier components are found by taking the absolute value-squared of the fast-fourier transform of the shifted and averaged spectrum.

$$\text{Cycles}=|\text{FFT(spec)}|^2$$

The Fourier components of only part of the shifted and average spectrum was used; specifically, the range from -170$\leq$v$\leq$800 km s^{-1} from figure 4.7. This was so that the main feature at $\sim$-210 and 840 km s^{-1} did not affect the analysis. These components are shown in figure 4.9. The number of components is equal to the size of the input array. The resulting fast-fourier transformed array is split in half - half being the power of each component of the spectrum, the other half being the mirror image of

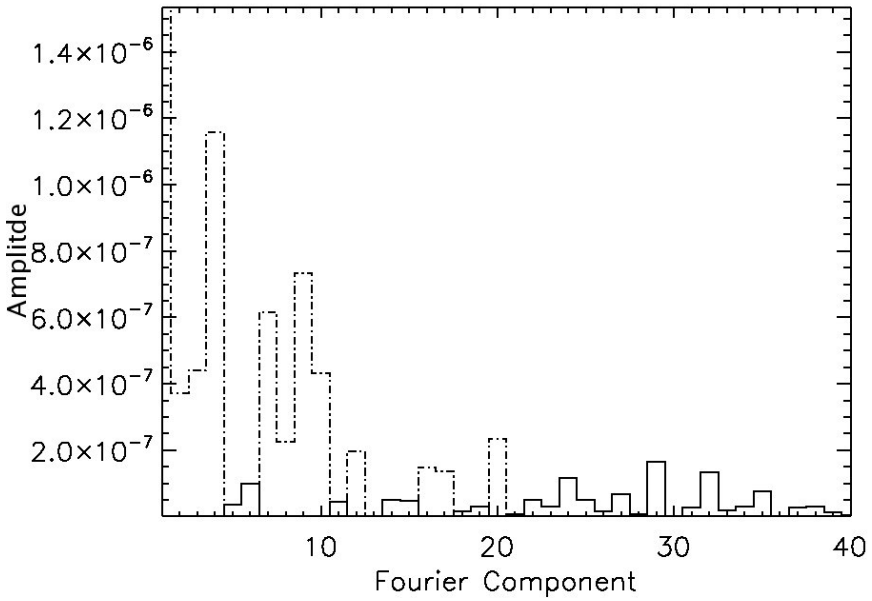

Figure 4.9 Figure showing the Fourier components of the shifted and averaged spectrum. The abnormally strong components below component 30 were removed. The range from 100 and above remains around the level of 20 to 40, up to the point where the fast-fourier transform mirrors and repeats the first components.

that. The strongest components suggest that there is a systematic frequency that exists throughout the shifted spectrum, which means it is a fringe component, and not that of the star. For example, the array shown is approximately 650 components, and from 60 to 325 (and the mirror image - 326 to 590), the power is on the order of that shown between pixel 60 to 100, around 10^{-7}. The spike in the low frequency components (that of less than 25) is a jump in around an order of magnitude or more. The components that were removed are shown in figure 4.9 as dot-dashed lines. These components were found by minimizing the appearance of fringes in the shifted spectrum of figure 4.7, while not taking out the random noise which is part of the real data.

The resulting corrected spectrum is shown in figure 4.10. It can be seen that the three-sigma level has dropped significantly. Specifically, the one-sigma level is now 0.15003%. This is significantly below what was found earlier using just the

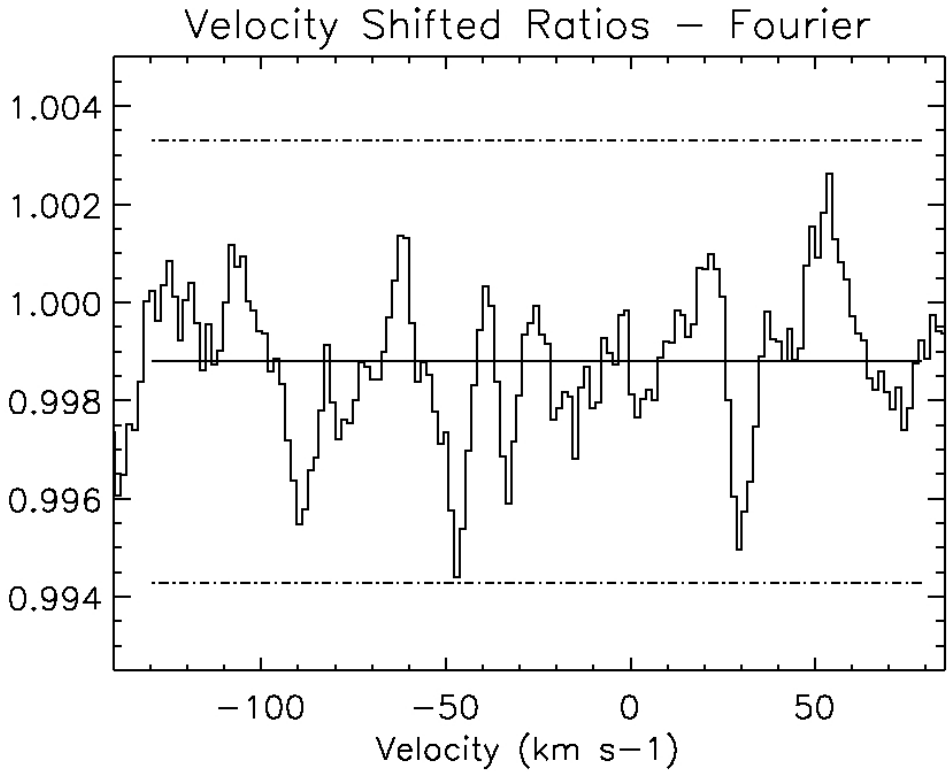

Figure 4.10 This shows the shifted average spectrum with the removed components. Again, the three-sigma level is marked by a dot-dashed line, while the average is shown by the solid line. The three-sigma level has dropped slightly compared to what was there with the shifted ratio.

raw average and even the shifted average of ratios. The final result of a standard deviation of 0.00150 will be the value that is used to calculate an upper limit on the column density of H_3^+ for the remainder of this chapter. With the ratio set around unity (approximately), the reciprocal of the standard deviation can be used to estimate a signal-to-noise ratio for the overall data set. This value comes out to be 667, which is closer to the estimated needed signal-to-noise of ∼2600 (calculated in section 4.6), but still fairly far away.

Each process described has been to extract as much information out of the available data as possible. Because the expected signal is so small, all of these

Process	1σ	3σ	S/N
Average (shifted)	0.00195	0.00586	512
Fourier removal	0.00150	0.00450	667

Table 4.1 Table showing a comparison of all of the data using the different techniques mentioned.

become necessary. The values of the standard deviation (one-sigma), three-sigma, and signal-to-noise for the different processes throughout are shown in table 4.1.

4.4 Equivalent Width Calculation

Now that the low one-sigma and three-sigma level has been quantified, it can be used to calculate an upper limit on the column density of H_3^+ in the atmosphere of HD 209458b. To do this, we need to find the equivalent width of a feature that would be the size of the level of one-sigma. This will be equated to the equivalent width of the H_3^+ feature, which can be solved for the column density.

The equivalent width given a specific column density can be found from the equation

$$EW = \frac{8\pi^3}{3hc}\,\tilde{\nu}\,N_{lev}\,|\mu^2| \tag{4.3}$$

where h is Planck's constant, c is the speed of light, $\tilde{\nu}$ is the wavenumber of the specific transition, N_{lev} is the number of molecules at a specific energy level, and $|\mu^2|$ is the dipole magnetic moment. Most of these quantities are given in the literature, such as the dipole magnetic moment (McCall 2001).

The equivalent width is also equal to a rectangle with a depth of 1 and width equal to the full width half maximum (FWHM) of the gaussian fitting the absorption feature that would be detectable at the one-sigma level.

$$EW = \sqrt{\pi}\,a_0\,a_2 \tag{4.4}$$

where a_0 is the standard deviation in the data and a_2 is given by:

$$a_2 = \frac{FWHM}{1.665} \tag{4.5}$$

$$FWHM = \frac{d\,\tilde{\nu}}{c} \tag{4.6}$$

where d is the dispersion of the instrument, $\tilde{\nu}$ is the central wavenumber of the line, and c is the speed of light. This will give a FWHM in units of wavenumbers, and thus a_2 and the equivalent width in units of wavenumbers as well.

4.5 Upper Limit Calculation

If the upper limit that will be calculated is low enough, it may rule out models predicted by Miller et al. (2000) and Yelle (2004). This would be extremely useful for those attempting to use the models to understand the mechanisms in the atmospheres of hot Jupiters. At this point, all of the necessary components to find an upper limit are known, so the calculation will proceed.

First, the equivalent width coming from a one-sigma feature using equation 4.4 can be equated to the equivalent width from a certain column density of H_3^+ in a specific level given by equation 4.3. Then, the equation will be solved for column density in terms of all known quantities. For this calculation, the R(1,0) feature will be used.

$$\sqrt{\pi}\,a_0\,a_2 = \frac{8\pi^3}{3hc}\;\tilde{\nu}\;N_{lev}\;|\mu^2| \tag{4.7}$$

$$\sqrt{\pi}\,\sigma\,\frac{d\,\tilde{\nu}}{1.665\,c} = \frac{8\pi^3}{3hc}\;\tilde{\nu}\;N_{lev}\;|\mu^2| \tag{4.8}$$

Leading to the final equation for the column density in terms of all known quantities.

$$N_{lev} = \frac{3\sqrt{\pi}\,\sigma\,h\,c\,d}{1.665\,c\,(8\,\pi^3\,|\mu^2|)} \tag{4.9}$$

$$N_{lev} = \frac{0.6\,\sigma\,h\,d}{\pi^{5/2}\,|\mu^2|} \tag{4.10}$$

In equation 4.10, σ is the standard deviation, d is the dispersion, and other variables are the same as earlier. Table 4.2 has all of the needed quantities for this calculation.

Transitition	σ	d (km s^{-1})	$\tilde{\nu}$ (cm^{-1})	$\lvert\mu^2\rvert$ (D^2)
R(1,0)	0.00150	6.5	2725.885	0.0259

Table 4.2 Table with the quantities needed for the upper limit calculation.

Using these quantities, an upper limit for the column density of the R(1,0) H_3^+ in the atmosphere of HD 209458b is

$$N_{lev} \leq 3.209 \cdot 10^{12}\ cm^{-2} \quad R(1,0) \tag{4.11}$$

Only the R(1,0) was used because the $R(1,1)^u$ fell into a telluric feature, making the one-sigma upper limit higher.

Now that the upper limit of column density has been calculated for each level, the total column density needs to be calculated. This will use the approximation of local thermodynamic equilibrium (LTE). It has been suggested that non-LTE effects are negligible for the temperatures of HD 209458b (Melin et al. 2005). The boltzmann equation can be used to find the total column density by:

$$\frac{N_{lev}}{N_{tot}} = \frac{g_i}{Z(T)}\, e^{-E/kT} \tag{4.12}$$

$$N_{tot} = \frac{Z(T)}{g_i} N_{lev}\, e^{E/kT} \tag{4.13}$$

Where Z(T) is the partition function as a function of temperature, E is the energy of the state, k is the Boltzmann constant and T is the temperature. The nuclear spin degeneracy g_i was set to 4 Rothman et al. (1992). The values for this equation are given in table 4.3.

By using values from table 4.3 in equation 4.13, the total upper limit of the column density can be found. Table 4.4 has the final estimates for the total column

Temperature	$\log_e$(Z)	E/kT (for R(1,0) line)
1400	6.113	0.08935
1600	6.372	0.07818
1800	6.605	0.06949

Table 4.3 Values for calculating the total column density of H_3^+ given the column density of the level. The partition function is given by Sidhu et al. (1992) and the value for the E is given as 86.9591 cm^{-1} by Lindsay and McCall (2001). The values for T were chosen as the effective temperature of the planet has been estimated between these values.

density given different temperatures. All of the values are around 10^{14} cm^{-2}, which is near the estimate of the highest predicted value of 10^{14} cm^{-2} (Miller et al. 2000).

Temperature	N_{tot} (cm^{-2})
1400	$3.964 \cdot 10^{14}$
1600	$5.077 \cdot 10^{14}$
1800	$6.353 \cdot 10^{14}$

Table 4.4 One-sigma upper limits for the R(1,0) column density in the atmosphere of HD 209458b.

4.6 Reverse Calculation

Just as an upper limit was calculated for a given signal-to-noise using PHOENIX, one can theoretically calculate the necessary signal-to-noise needed in order to detect theoretical column densities. Miller et al. (2000) predict a higher column density, so the necessary signal-to-noise ratio will be calculated using this value to check the current result. In principle, one could calculate the same thing for a lower column density, but will lead to a higher necessary signal-to-noise.

We will begin with the predicted column density of H_3^+ being 10^{14} cm^{-2}. However, this is the total column density, which must be translated into an estimate

for the column density of a given level. For the purposes of this calculation, the R(1.0) state will be used as this has the stronger transition. Assuming a temperature of 1400 K, the column density in a certain level will be described by:

$$\frac{N_{lev}}{N_{tot}} = \frac{g_i}{Z(T)}\, e^{-E/kT} \tag{4.14}$$

$$N_{lev} = \frac{g_i}{Z(T)} N_{tot} e^{-E/kT} \tag{4.15}$$

$$N_{lev} = 8.099 \cdot 10^{11} cm^{-2} \tag{4.16}$$

This equation can now be used in equation 4.3 to calculate the necessary S/N to measure the column density of H_3^+ given the same setup. This time, however, the equation will be solved for the standard deviation rather than the total number column density.

$$\sqrt{\pi}\,\sigma\,\frac{d\,\tilde{\nu}}{1.665\,c} = \frac{8\pi^3}{3hc}\;\tilde{\nu}\;N_{lev}\;|\mu^2| \tag{4.17}$$

$$\sigma = \frac{8\;1.665\;\pi^{5/2}}{3\,h\,d\;\;N_{lev}}\;|\mu^2| \tag{4.18}$$

Using the equation for the number in a single level, the necessary standard deviation to detect that level is:

$$\sigma = 3.78 \cdot 10^{-4}. \tag{4.19}$$

This can be used to find the signal-to-noise necessary, and if the ratio is set to unity, can be equated as:

$$\frac{S}{N} = \frac{1}{\sigma} = 2645 \tag{4.20}$$

Because the standard deviation calculated earlier is $1.50{\cdot}10^{-3}$, this is a good check to show that the calculated standard deviation from the data is below the necessary value to detect the column density predicted by (Miller et al. 2000). In other words, the R(1,0) feature is expected to be $\sim$0.04% deep, which is less than an order of magnitude below our current upper limit.

4.7 Limits of Technique

While the resolution of PHOENIX is extremely high (∼45,000) there are still limits using the Gemini South telescope. First, and most noticeable in the data, is the atmosphere. Water in the atmosphere becomes very "bright" at infrared wavelengths. This reduces the overall quality of data, as the noise from the atmosphere increases. This is clearly seen in figure 4.11, where a modeled atmosphere from Gemini South in Chile is compared to the Keck Telescope in Hawaii. Keck has a much higher altitude and therefore has a much lower column density of water to look through, meaning the overall noise is lower.

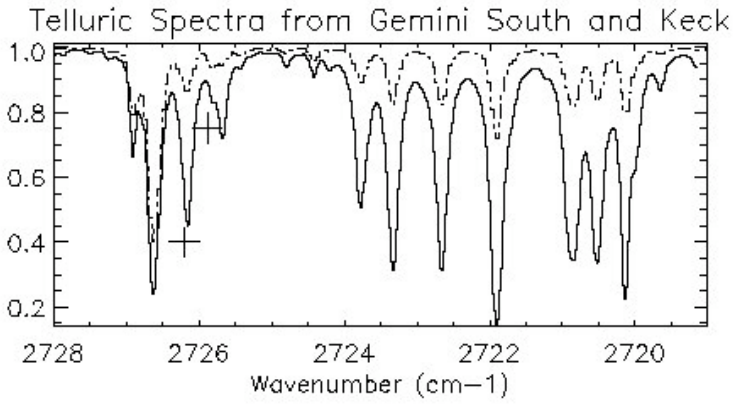

Figure 4.11 Comparison between the telluric spectrum at Gemini South (solid line) and Keck (dashed line). The normalized intensity is plotted versus wavenumber. The location of the R(1,0) and R(1,1)^u features are shown as pluses. The striking difference between the depths of the two spectra comes from water in Earths atmosphere (∼55% transmittance at Gemini South compared to ∼87% at Keck for the R(1,1)^u feature).

4.8 Necessary Integration Time

With the knowledge that the current upper limit is a factor of ∼4 greater than what is needed to rule out predictions, how much more integration time is necessary? If the standard deviation went as $\sqrt{N}$ (which is an optimistic estimate

because of the increased difficulty of removing small components affecting the ratios), then 16 more transits would need to be observed in order to reach the needed standard deviation. Thus, with this current technique at the current instrument, this seems unattainable.

CHAPTER 5

FUTURE

This project has plenty of work that can be done in the future to improve the upper limit or possibly make a detection. There is still data that is still to be reduced from Keck, which is promising due to the improved atmosphere (see section 4.7). There are two transits of observations in a different band that can add to previously reduced data to possibly make a detection, or at least decrease the upper limit that has been calculated.

5.1 NIRSPEC Observations

There are still observations from 2004 which utilize NIRSPEC at Keck. Two transits (June 8 and June 15) were observed. These observations are in the K-band and are searching for the Q(1,0) transition. Despite being an overtone transition, the strength is only seven times weaker than the fundamental transitions (McCall 2001). Thus, it only takes a few more optical depths, which would be achieved in the atmosphere of an exoplanet, to not have a noticeable difference between the fundamental and overtone transitions.

Starting with equation 4.3, one can find the equivalent width and therefore the standard deviation necessary to detect an H_3^+ signal. This can also be compared to the equivalent width and necessary standard deviation for the R(1,0) lines. The Q(1,0), at 4907.8 cm^{-1}, has an equivalent width (given the prediction of 10^{18} cm^{-2}) of 3.149x10^{-5} cm^{-1}. This is about three times that of the R(1,0) line. This means that the standard deviation necessary to detect a signal becomes is described by:

$$\sigma = \frac{EW\ 1.665\, c}{\sqrt{\pi}\, d\, \nu_c}, \tag{5.1}$$

where c is the speed of light, d is the dispersion of the instrument (12 km s^{-1} for NIRSPEC), and ν_c is the entral wavenumber of the band (4884.1 cm^{-1} for the K-band on NIRSPEC). When plugging in these values and the equivalent width

calculated earlier, the standard deviation becomes:

$$\sigma = 1.5 \cdot 10^{-4}, \tag{5.2}$$

which translates to about 0.015%. This is comparable to what was found earlier, so the K-band data is not much of a loss (in terms of the spectral grasp and instrument dispersion).

5.1.1 Initial reduced spectra from NIRSPEC

These data have yet to be reduced entirely, however an initial comparison to what was done in chapter 4 can still be made. Similar steps will be shown to get an idea of how these data compare. However, it should be noted that during the reduction, it was obvious that in the region where the Q(1,0) absorption feature is expected, the atmospheric model was not as accurate for the small features dominating that area of the spectrum. This could be because the model is not sophisticated enough to get to the necessary signal-to-noise. A standard star could not be used in the reduction of the PHOENIX data because those data were from a lower altitude where minute to minute changes in the atmosphere were dominating the telluric features. Therefore, a standard star taken before or after (or both) would not have created for an accurate fit of the telluric features. In the K-band, however, the atmosphere does not produce as much noise. Similarly, the higher altitude means that there is less atmosphere through which to look at the site of NIRSPEC, then at Gemini South. These two factors suggest a standard star would fit well for these data where the telluric model is not as accurate.

To begin, figure 5.1 shows a single frame from the night. The most noticeable difference are the powerful telluric features towards the red (right in figure 5.1) end of the spectrum. Fortunately, the Q(1,0) feature (shown as the two crosses) does not fall in one of the deep features, but rather in the somewhat "calmer" part of the spectrum.

After fitting the telluric model to each of the 21 sets lasting 8 minutes each, ratios for each set were created. Just as in chapter 4, the ratio was created by

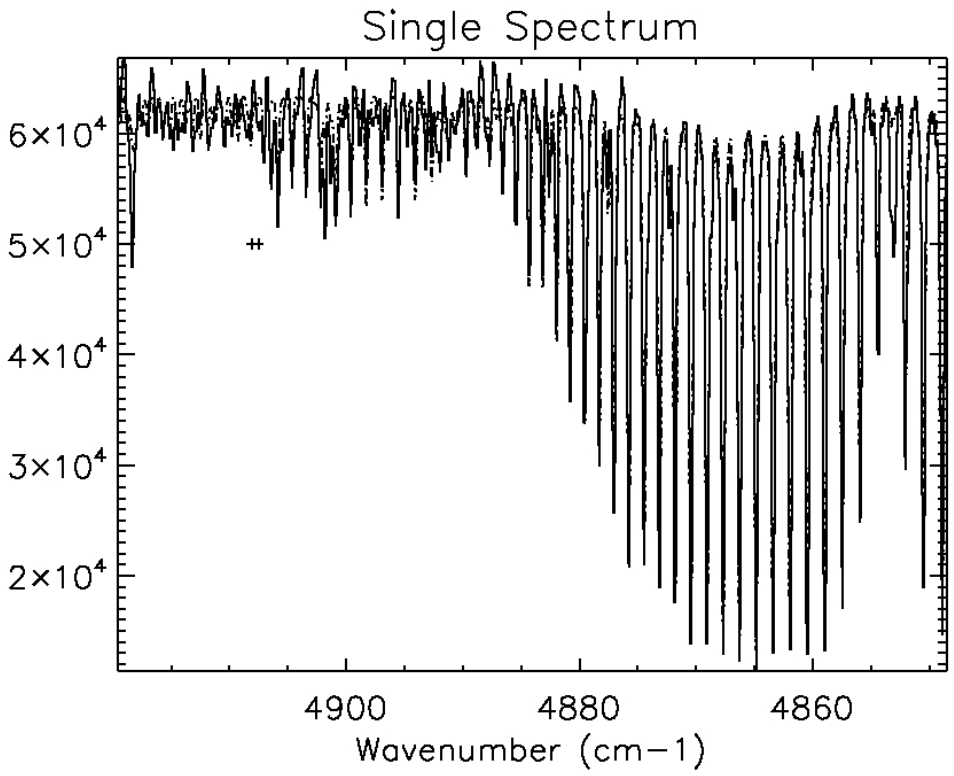

Figure 5.1 This shows single ABBA frame from the NIRSPEC observations. Note the difference between this and figure 4.1. This is because the NIRSPEC observations are in the K-band, whereas the PHOENIX data were in the L-band. The crosses show where the Q(1,0) feature resides, the spacing being the effective doppler shift over the course of the observations. Fortunately, the Q(1,0) feature is not in the extremely strong telluric features towards the red (right) side of the spectrum.

dividing the science data by the telluric model. These ratios were then averaged together to produce figure 5.2. The overall averaged ratio is more "well-behaved" than the PHOENIX data; meaning the overall ratios are near unity and have no significant dips or trends. A closer view of the average ratio is shown in figure 5.3. The crosses show the effect of the doppler shift throughout the night.

Despite the fact that the ratio is much cleaner overall than the previous data, there is a much more distinct fringing pattern appearing throughout the spectrum. This is especially obvious for wavenumbers greater than 4875 cm^{-1}. This effect

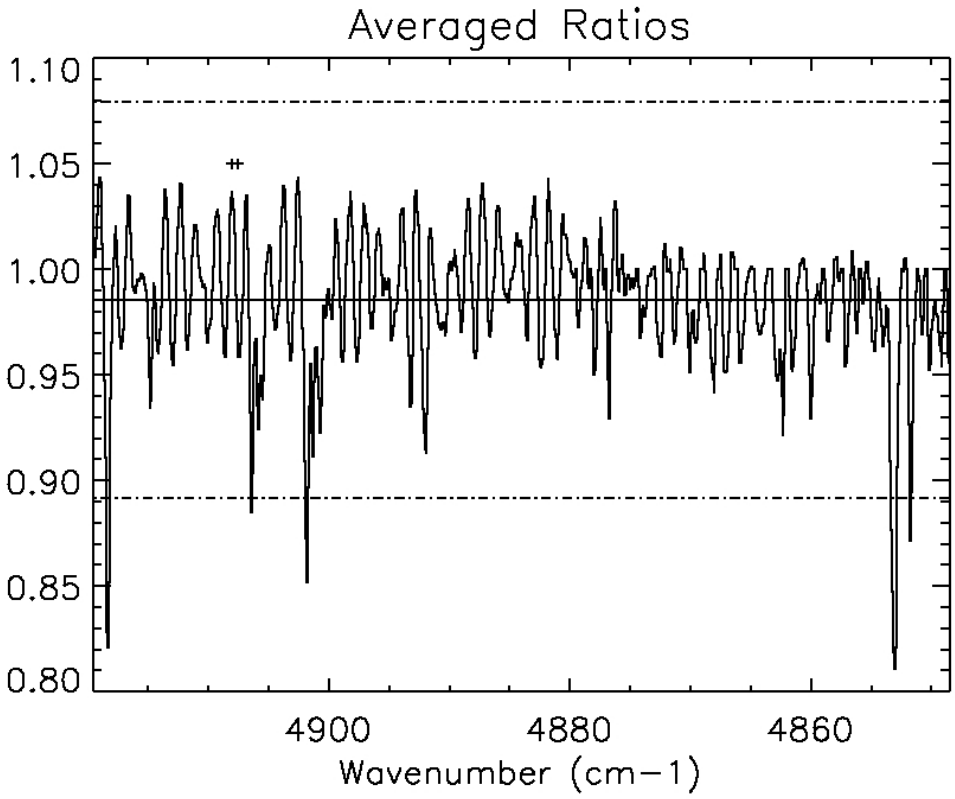

Figure 5.2 This shows the average of all of the ratios (science data divided by telluric model) from the June 15th observations, which consisted of 21 ABBA sets. There appears to be a fringing pattern, manifesting as a periodic function throughout the ratio, which can be partially removed through fourier analysis. The crosses show the location of the Q(1,0) line (with doppler shift throughout the observation), while the dot-dashed lines show the three-sigma limits.

can be partially removed similar to those of the PHOENIX data, by way of fourier analysis. This is distinctly shown in figure 5.4, where the power of the components near 26 and around 33 are much higher than the rest of the spectrum. It should be noted that the power of the rest of the components are of the order of those seen between components 40 and 50. The spikes in the power come from increased contributions of those frequency components to the ratio average spectrum.

The effect of the de-fringing is seen in figure 5.5, where the de-fringed spectrum is shown with the original spectrum over-plotted. The old spectrum is shown

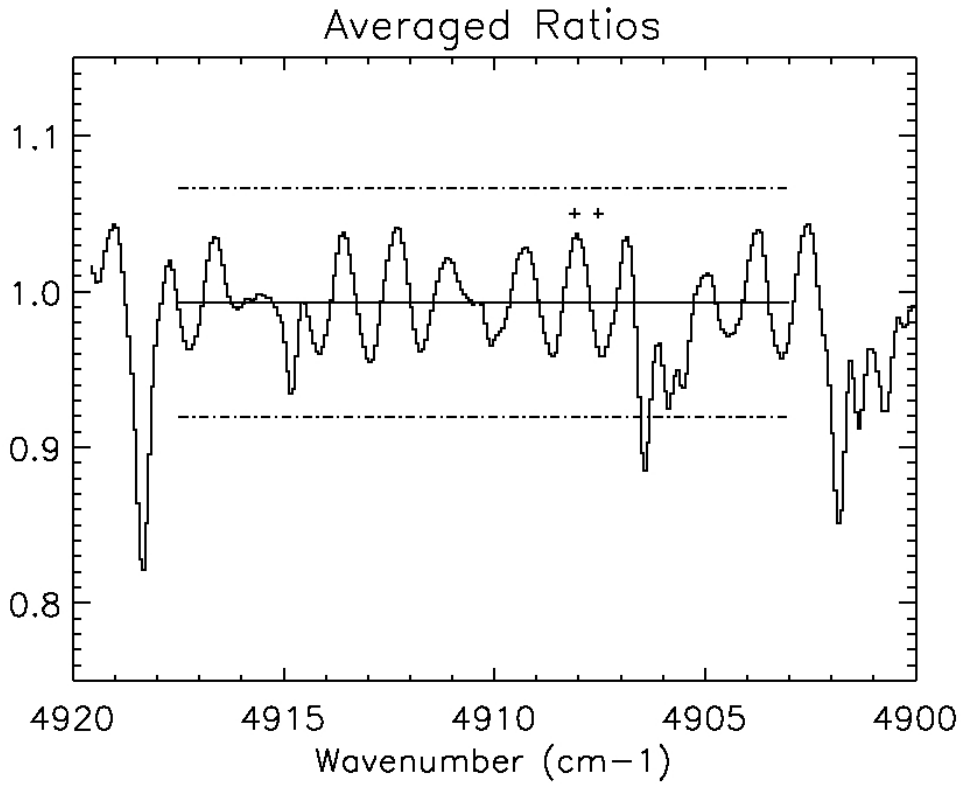

Figure 5.3 A closer view of figure 5.2. The dot-dashed line shows the three-sigma limit over which the range is plotted, without including the feature at 4906.5 cm^{-1}. The one-sigma limit is not as small as the PHOENIX data, but this analysis is just to get an idea of the quality.

as the dot-dashed line with the three-sigma limit shown as the dashed horizontal line. The crosses are where the Q(1,0) feature is expected throughout the night's observation. After de-fringing, more the true science data come through while the fringing pattern is removed. The new, three-sigma limit is shown, which is a factor of ∼2 better than what the previous limit would be.

The de-fringed spectrum is shown in figure 5.6 alone, with a closer view in figure 5.7. There are some features that need to be explored further to determine the cause, such as the ones near 4902 and 4907 cm^{-1}. These features could be artifacts from the fourier analysis, from a bad atmospheric fit, or even from a few bad spectra that were included into the average.

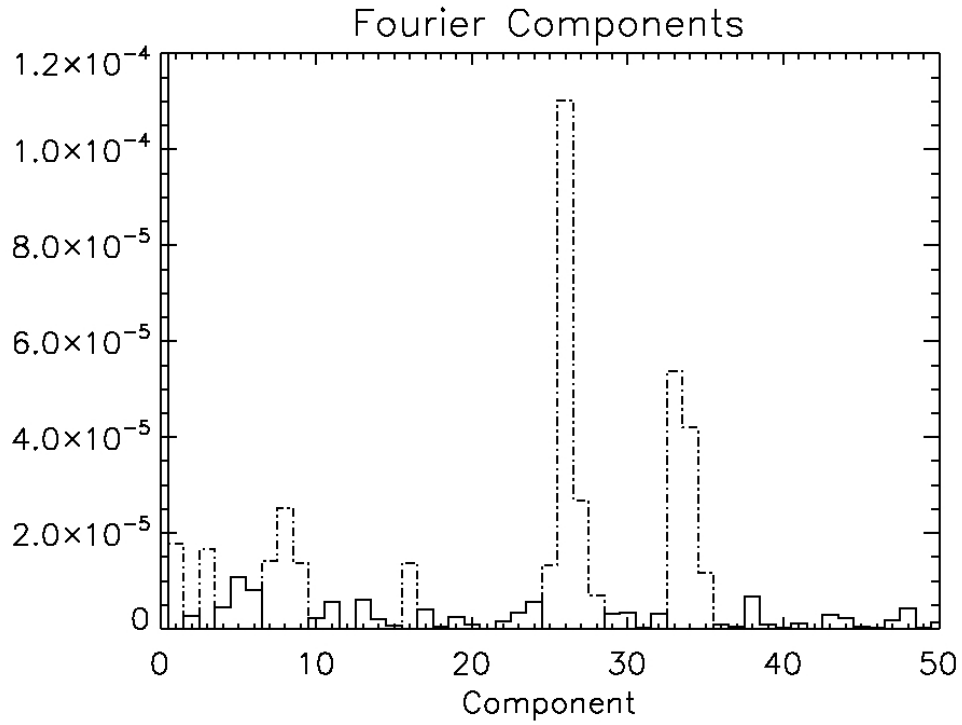

Figure 5.4 The fourier components of approximately half of the spectrum shown in figure 5.1, so as not to include the strong telluric features in the analysis. The most powerful components were removed (shown as dot-dashed line). This should remove a large amount of the fringing seen in figure 5.2. The power of the components past 50 are of the same order as the power of the components from 40 to 50.

From this initial rough analysis, the one-sigma level is somewhere around 1.5%. This is an order of magnitude higher than that found from the rigorous reduction, but that has not been done fully here. The reason for going through this initial reduction is to get an idea of the quality of data that exist with these observations. It seems that these observations can be combined with earlier observations to at least reduce the upper limit. With a similar rigorous reduction of these data, one hopes to find comparable signal-to-noise.

These data still need to be shifted for both the doppler shift throughout the observation and for the shift of the geocentric velocity of the host star. Future

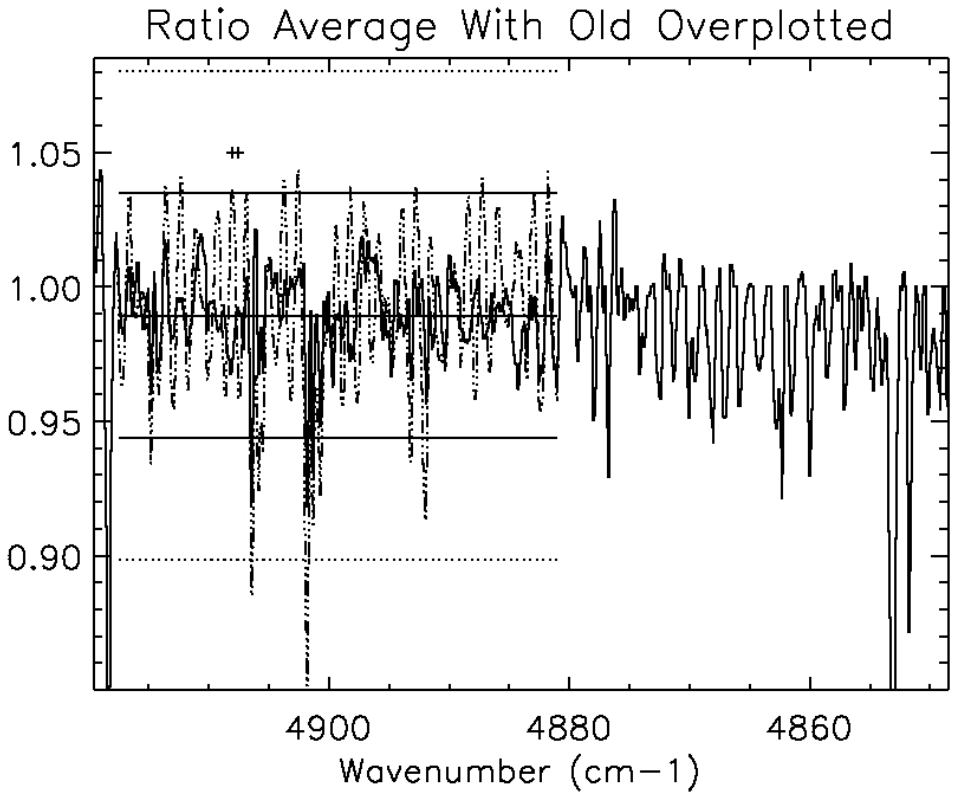

Figure 5.5 This shows the result of the de-fringing by removing fourier components. The dot-dashed line shows the previous averaged ratios, while the solid line shows the de-fringed ratio. The three sigma levels are shown before (dot-dashed horizontal lines) and after the de-fringing (solid horizontal lines), plotted over the range from which they were calculated. The three-sigma limit has improved by approximately a factor of two. The triangle shows location of the Q(1,0) feature.

analysis will also use a standard star to see if the atmospheric fit is better. If so, the three-sigma limit may be decreased further, perhaps comparable to that found in chapter 4. Also, there is still an entire night of data that still require attention. With the combination of these three nights (one from PHOENIX, two from NIRSPEC), perhaps the signal-to-noise will be enough to make a lower upper limit, or, perhaps, even a detection.

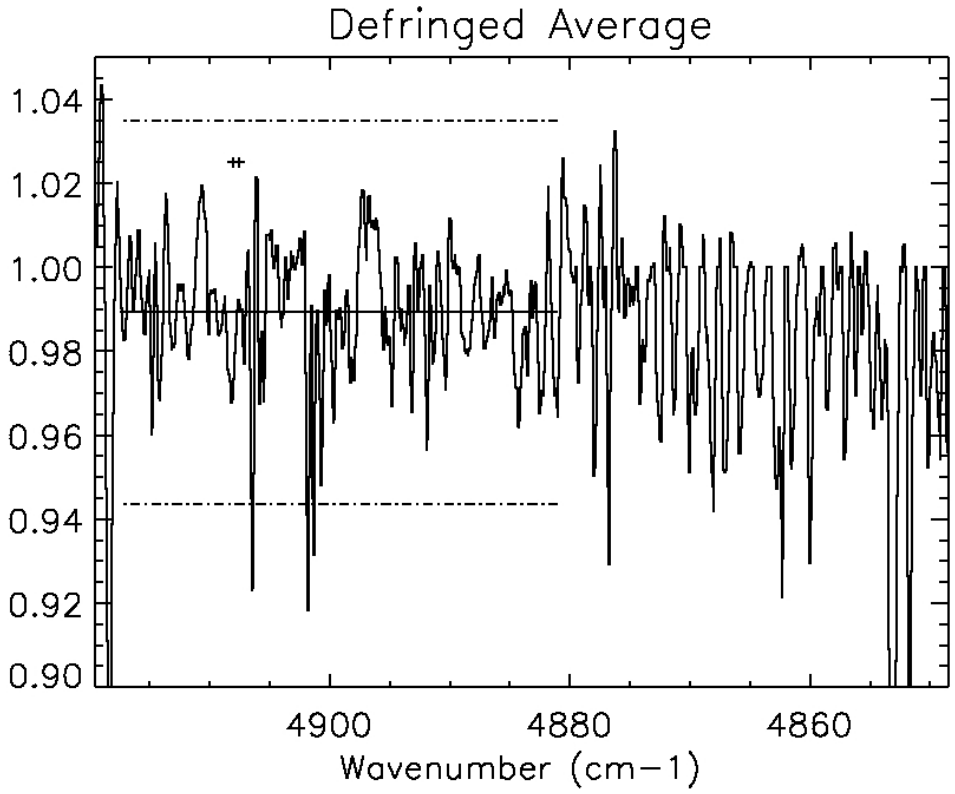

Figure 5.6 This shows the resulting ratio average after de-fringing, without the old average over-plotted. Note the difference between the spectrum from the left side of the spectrum, where the de-fringing was done, and the right side, where there was no de-fringing.

5.2 Other Molecules

5.2.1 H_2

Molecular Hydrogen (H_2) is the most abundant molecule in the atmospheres of exoplanets. However, H_2 is very difficult to detect. First, as the near infrared ro-vibrational transitions are relatively weak. The best transitions to observe for the temperature of the planet are in the mid-infrared, which has a much higher telluric signature than the bands used in the presented data. Therefore, detection of molecular hydrogen from the ground is extremely difficult. Similarly, ultraviolet radiation dissociates H_2 effectively, which in the atmosphere of HD 209458b, would

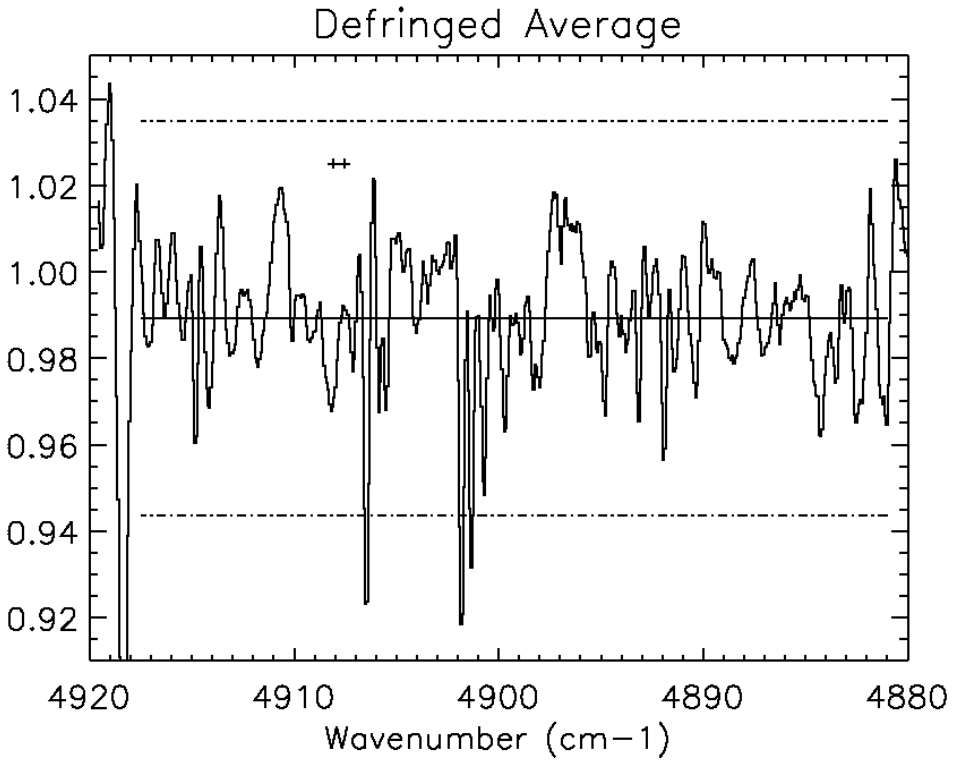

Figure 5.7 A closer look at the de-fringed average of the ratios.

be prominent. This is expected, as ionized H_2 is what creates H_3^+ in the first place. For these reasons, H_2 is not a useful molecule to observe in the atmospheres of hot Jupiters like HD 209458b.

5.2.2 CO

To date, there has not been a ground-based detection of an exoplanetary atmosphere. CO proves to be a good candidate to attempt a ground-based detection for many reasons. First, its transitions are in a relatively clear telluric window at 2 μm. Second, it has been suggested that mixing would provide an increased abundance from what models have predicted (Seager and Sasselov 2000).

Unfortunately, current searches for CO have been unsuccessful (Deming et al. 2005a). The explanation is that silicate clouds exist at a higher altitudes than

previously thought. When observing in transit, the atmosphere is optically thick out to a larger radius, meaning that the observable column density would be much less. Silicate in the clouds would fortuitously explain a lower detection of Sodium than expected for the same reasons as the non-detection of CO (Deming et al. 2005a).

5.3 Final Remarks

At this point it is advantageous to review the reasons for searching for H_3^+ in the atmosphere of an exoplanet. If H_3^+ was detected, it would mark the first ground-based detection of an exoplanetary atmosphere. This would show that such a measurement would be possible with current technology. As we have not made a detection, but rather found an upper limit, suggestions of the necessary future technology to make a detection can be made instead. For example, one of the limiting factors in the reduction for the PHOENIX data was the very accurate modeling of the telluric features. So, if better models exist, the limits could be constrained even further. Along those lines, it seems that even a higher resolution instrument at the central wavenumber would not improve things very much. The resolution would need to improve by an order of magnitude to reach the predictions of Miller et al. (2000), or ∼250,000. For the near-infrared, this has not, in practice, been realized yet.

Similarly, if a detection was made, it would be used to calibrate models. Despite being very strange worlds - Jupiter-sized planets at 0.05 AU from their host star - the atmospheres still have the same components we expect from our own Jupiter, from which models can be created to estimate what would be observed at Earth. Perhaps next-generation telescopes can approach this limit.

5.3.1 Weather/Clouds

It is debatable how the detection of H_3^+ is affected by clouds in the atmosphere of exoplanets. Certainly, it seems that as H_3^+ is a component of the ionosphere, the clouds would have to be at a high altitude to have a dramatic effect.

However, can an upper limit, or non-detection place some constraints on the altitude or breadth of clouds? Perhaps further analysis, or collaboration with modelers of exoplanetary atmospheres, can improve the null result into a useful contribution to models.

5.3.2 Atmospheres of Earth-like Planets

The ultimate goal of studying exoplanetary atmospheres, one might argue, is to eventually be able to detect components of Earth-like planetary atmospheres. However, the atmospheres of "hot" Jupiters are trivially simple to detect, relative to that of an Earth-like planet at around 1 AU from the host star. Also, even though there are detections of atmospheres of a few exoplanets, they are not extremely well understood. "Understanding" in this case refers to knowledge of how the components of the atmosphere connect to observational predictions. Thus, being able to understand the atmosphere of an Earth-like planet is currently a lofty goal. This is not to say that such an understanding is impossible, but with current technology seems out of reach.

5.3.3 Life?

There seems to be one huge question that all studies of astrobiology (which also could be used to label this thesis) are trying to address in some way: is Earth the only planet with life?

Previous attempts to detect life have been passive searches, such as the Search for Extra-Terrestrial Intelligence (SETI), where the presence of life would be detected by receiving signals. The success of the SETI program relies on many assumptions on intelligent life being similar to humans. A more realistic way to answer the question of life existing elsewhere is to actively search for forms of life, rather than being passive. This does not require intelligent life to exist, only requiring that life has some sort of detectible signature that could be observed, known as a biomarker. For life similar to what we know on Earth, these biomarkers could be ozone (O_3), carbon dioxide (CO_2), water (H_2O), and methane (CH_4), but are not

limited to just these (Des Marais et al. 2002). Just to note, these refer to familiar and recognizable life, and does not take into account more exotic forms that may exist.

If biomarkers reflect life on Earth, then to detect biomarkers on other exoplanets, Earth-like planets will most likely be the planets one would want to observe. Therefore, before detecting biomarkers, detection of nearby Earth-mass planets must be the first step. Similarly, to detect atmospheric components of these Earth-like planets, the methods and technology to detect such components in the atmospheres of exoplanets must be robust. This is where this thesis contributes - answering the question of whether atmospheric components can be detected from the ground. If so, what does this tell us about the atmospheres of hot Jupiters, which are currently the only exoplanet atmospheres which we can study. If a detection cannot be made, what does that tell us, if anything about the atmosphere? What future technology would ensure a successful detection?

Future missions such as the Space Interferometery Mission (SIM) and Terrestrial Planet Finder (TPF) are just two of many that will attempt to detect lower mass planets and observe their atmospheres. As the launch dates for these missions are far off into the future, it seems that these issues will not be addressed soon. However, as radial velocity surveys continue, smaller planets further from their host stars will be discovered. As transit studies become more robust, characteristics of exoplanets will become more complete. And as microlensing surveys are completed, the likelihood of a planet existing around a star will be constrained. With all of these contributions, which will come before the space-based missions mentioned, our basic knowledge of exoplanets and their characteristics will increase dramatically. This knowledge will guide next generation telescopes that will improve detection and characterization of exoplanets and their atmospheres.

Does life exist elsewhere in the universe? This extremely large and meaningful question is often ignored because of its grandiose nature. However, for the first time in human existence, this question can *realistically* be approached, and possibly answered.

APPENDICES

Appendix A

DATA REDUCTION

This section will outline the general data reduction algorithm used to reduce the NIRSPEC data used in this thesis. The algorithms were inherited from Dr. Sean Brittain (Brittain et al. 2003) and have been slightly tweaked to address the specifics of this project.

A.1 Reduction Routines

Listed are the programs with short descriptions of the main routines and commands used to convert ccd fits images into the spectra presented in this thesis.

A.1.1 @b1_4disps

This is the main "batch" program which reads in the flat files, dark files, as well as ABBA frames for reduction. The files are read in, flat fielded and dark subtracted, and then the frames are subtracted: $(A_1\text{-}B_1\text{-}B_2\text{+}A_2)/2.0$. This is to subtract sky emission.

The frame is presented to the user, an based on mouse clicks along both the A and B line, a polynomial is fit. This is to find the science spectrum along the chip, and to straighten the spectrum along the chip. Figure A.1 shows a screenshot of the ABBA frame presented to the user, with the A beam already selected.

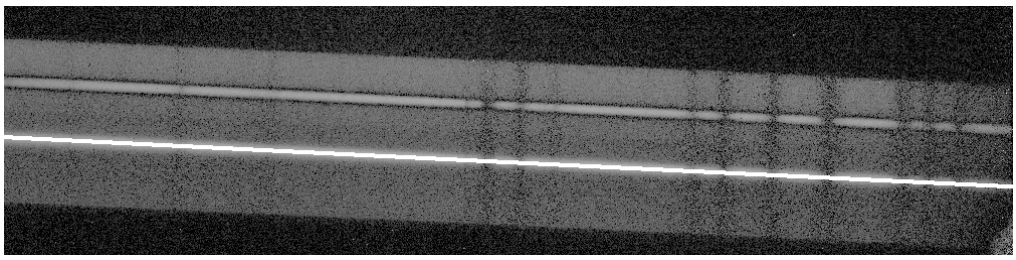

Figure A.1 Screenshot of ABBA frame, from which the A and B beams are selected. Here, the A beam has been selected (shown as the white line).

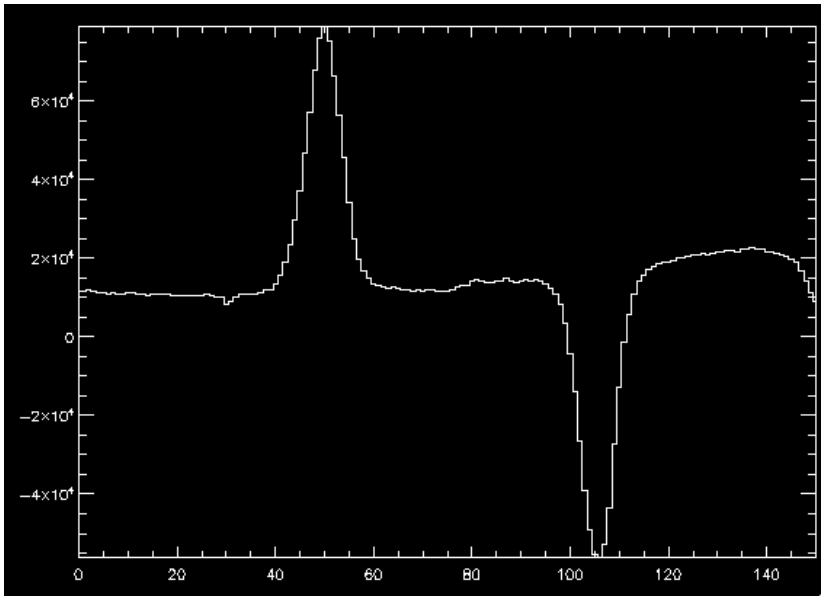

Figure A.2 A screenshot of the sum of the columns along the straightened spectrum. Here the A and B beams are clearly seen as the gaussians above and below the continuum. The reason for the negative B beam comes from the subtraction mentioned earlier.

At the end of this program, the beams have been straightened, and the sum of the columns are presented to the user. A sample is shown in figure A.2.

A.2 addrows_nod_nir

After the beams have been straightened, the rows that contain the A and B beams need to be selected. Using figure A.2, the rows can be "added" to the reduction routine, which is the function of this program.

A.3 deslope_opt_nir

This program takes the science data selected from the A and B beam rows, sums along those rows, to produce a spectrum. This spectrum will be fit to the continuum and later will be fit to an atmospheric model to remove telluric features.

While fitting to the continuum, the telluric features should not be taken into account. For this, the user selects out sections of the spectrum where telluric features dominate, shown in figure A.3.

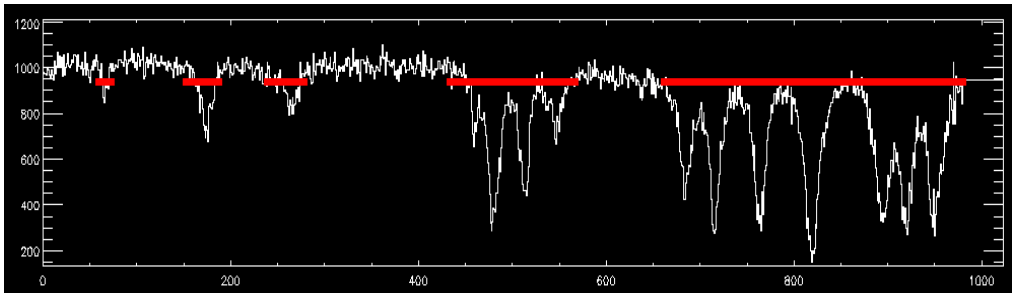

Figure A.3 Screenshot of program where the telluric features are ignored to fit to the continuum. The features omitted are marked in red.

After the telluric features have been omitted, the continuum is fit to a polynomial of the user's choosing. A low order polynomial (2^{nd} or 3^{rd} order) is usually good enough to fit to the continuum. The fit and resulting "de-sloping" (dividing by the fit), is shown in the two frames of figures A.4

A.4 readatm_2disp2_big

The last program to run fits the telluric model to the data. A screenshot of such a fit is shown in figure A.5. The residuals of the fit are shown in the bottom frame. The model dispersion is adjusted to fit the data in order to get a de-sloped spectrum, model fit, but just as important, a frequency calibration. This is the final formal program in the reduction process, and after this all of the necessary tools for further reduction have been created.

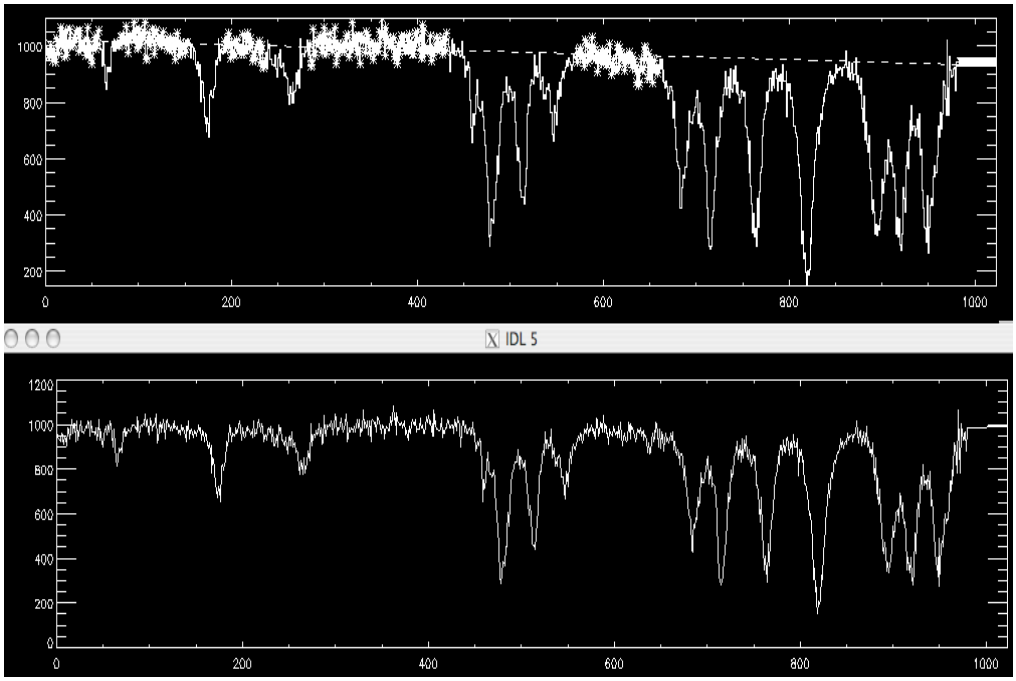

Figure A.4 Screenshot of the continuum points fit in order to de-slope the spectrum. The top frame is the fit (dashed line), while the bottom frame shows the resulting de-sloped spectrum.

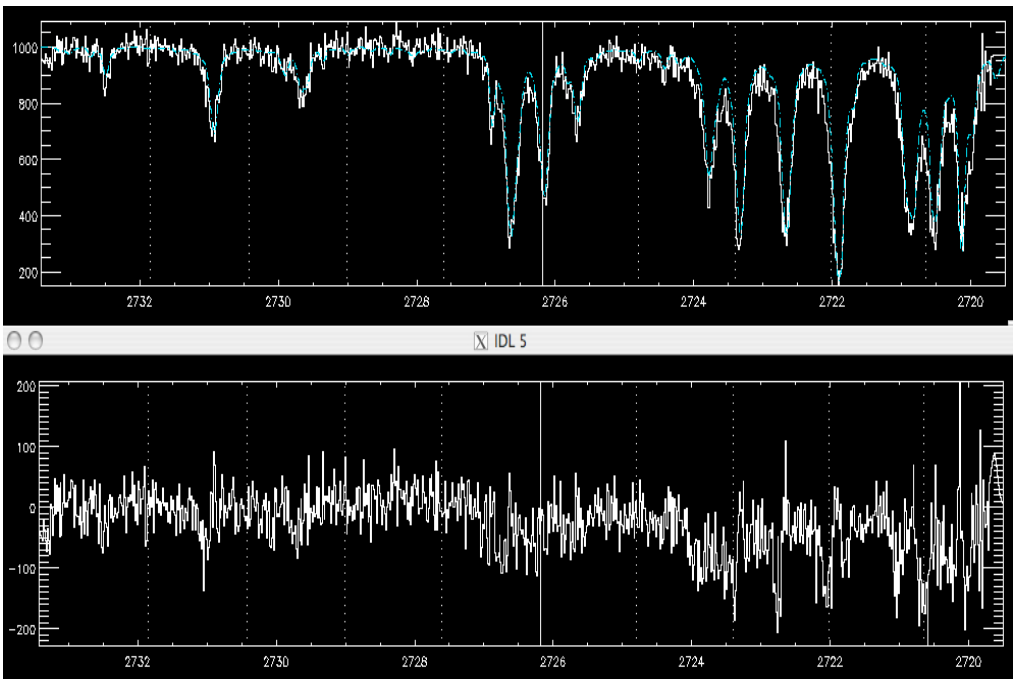

Figure A.5 Screenshot of the telluric model fit. The model is shown as the blue dot-dashed line

Appendix B

VELOCITY SHIFTING

This section is to show why velocity shifting of single frames over the course of a planetary transit is necessary. This will be done by using the Interactive Data Language (IDL) to create sample spectrum with an imbedded absorption feature. The imaginary planet will have a small absorption feature that may be buried in noise for a single frame. The goal would be to "tease out" a detectible signal. This may be more complicated than just observing for long periods of time and adding up the individual frames. Ideally, the reduction should include the planetary motion across the face of the host star, which increases or decreases the line-of-sight velocity and doppler shifts any line attributed to the planet.

B.1 Setup

To begin, a twenty frames consisting of a 100 pixel spectrum were created. Each frame had a signal-to-noise ratio of 50 (which is just $1/\sigma$ for a continuum ratio of 1). The frames are similar to reduced ratio spectra shown earlier, where the signal was divided by the model. In this simulated spectrum, an absorption feature was subtracted out for each frame. This absorption feature was set to a gaussian 2% deep, centered on the 50th pixel, with a total width of 10 pixels.

B.2 A Single Frame

Figure B.1 shows a single frame with an absorption feature. A feature is not noticeable around pixel 50 beyond the 3σ line, meaning there is no detection. Moreover, there isn't even a hint of a feature within the dot-dashed lines.

To account for a doppler shift, each frame's feature was shifted one pixel, depending on how far it was from the center of the transit (which was frame 10). For example, frame 9 had the center of the feature shifted one pixel to the left, and frame 13 had a three pixel shift to the right. This linear shift is not entirely accurate, but for the purposes of this exercise will be a good representation.

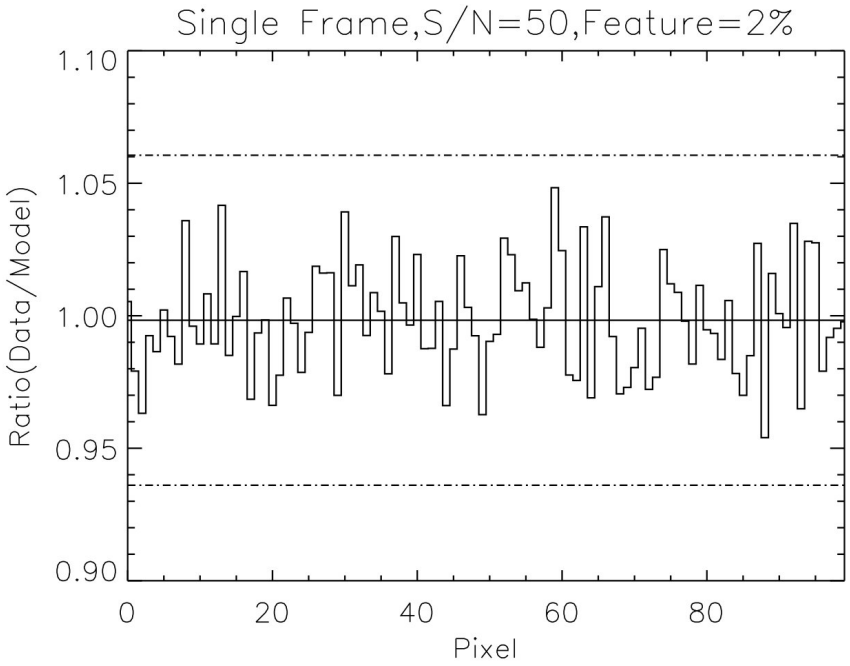

Figure B.1 Here is a single normalized frame with a S/N of 50, with a 2% absorption feature. The solid line is the average, and the dot-dashed lines represent 3σ deviation from the mean. There is no discernible feature here, which is a 10 pixel feature centered at pixel 50.

B.3 Adding Frames

To show that just adding single frames would not necessarily give a 3σ result, the frames were stacked. Adding frames increases the S/N (decreases the standard deviation) as $\sqrt{N}$, where N is the number of frames that have been stacked. This is shown in figure B.2, where the standard deviation is shown against the number of frames that have been added. Adding together the first and second frame provides great improvement, whereas adding the 20th frame to the first 19 frames combined does not give the same amount of improvement in the S/N ratio. The end result of the 20 frames is a S/N$\sim$225, much greater than the initial S/N=50.

One might think that stacking 20 frames, even without correcting for the velocity shifts, should produce a detectible result, perhaps not at a 3σ level, but such that it would be visible in the stacked spectrum. Figure B.3 shows that this is

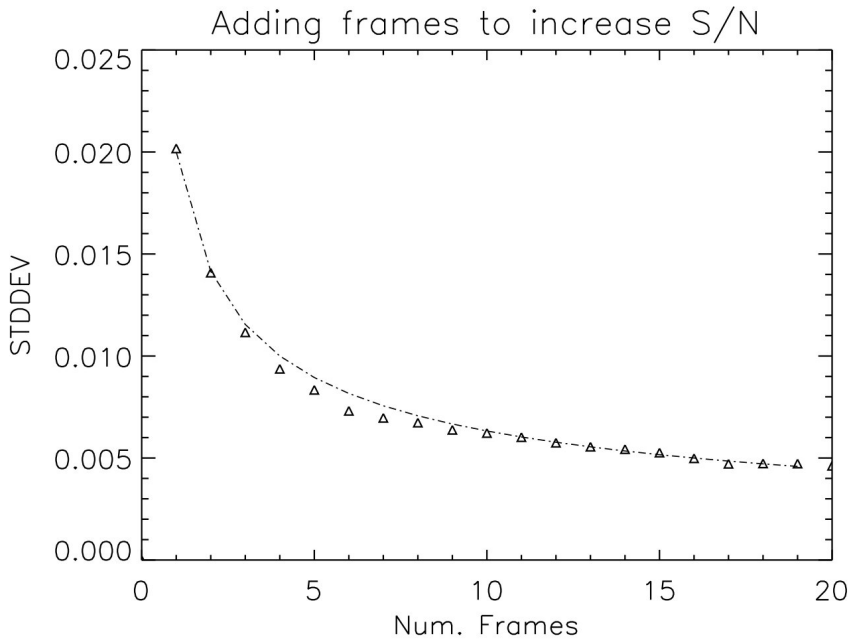

Figure B.2 This shows a standard deviation ratio for frames when adding adding. When adding more frames, the ratio goes as $1/\sqrt{N}$, which is the dot-dashed line.

not the case. While the standard deviation has decreased dramatically, the feature has been "smeared out" over the 20 frames, making it seem as though there is no feature at all. This shows why a correction for the doppler shift is necessary.

Shifting is especially important if placing an upper limit on the amount of material that should produce a feature. Without shifting, an upper limit could be placed at the 3σ level, or around 1.5%. However, with the information known by setting up the problem, there is in fact a 2% deep feature. This would be especially damaging if someone later analyzed the same object, but correctly shifting, and found a feature above the upper limit placed through this analysis. This would have a similar detrimental effect if someone used an upper limit in modeling the atmosphere of the planet, who might use the upper limit to refine simulations, which could predict erroneous results for other atmospheric properties.

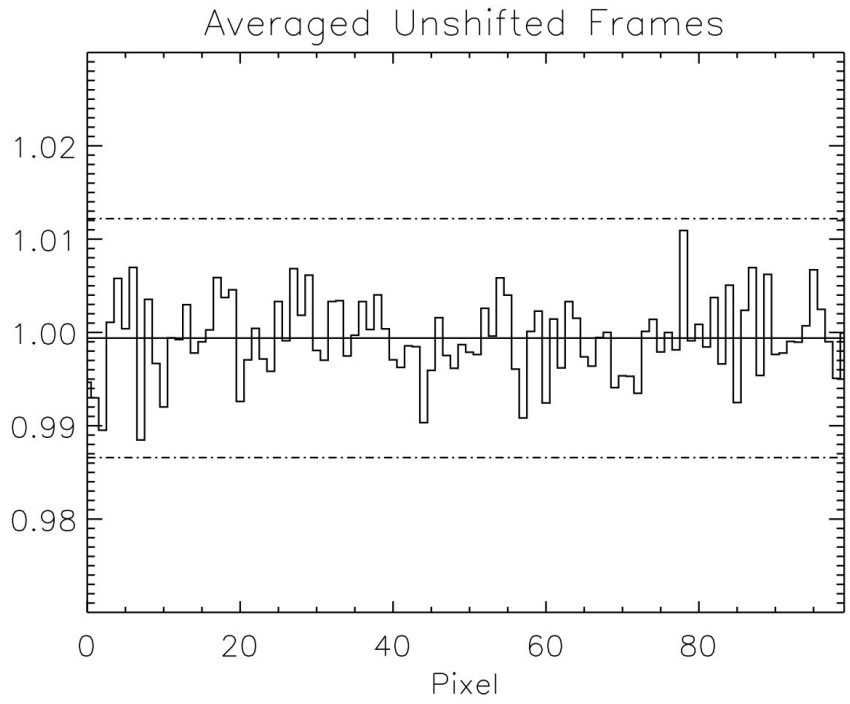

Figure B.3 This is the result of the unshifted 20 frames stacked together. Still, there is not a 3σ detection, even though the overall signal-to-noise has increased.

B.4 Shifting Frames

Finally, when shifting the frames back to the rest wavelength (pixel 50, in this case), a distinguishable feature emerges. Figure B.4 shows this shifted spectrum, with a clear feature peaked at pixel 50, beyond the 3σ limit. Also, the depth of the feature is $\sim$2%, which is what the feature was set to be originally.

Therefore, it can be seen that velocity shifting is a necessary step in the reduction process, at least to make a detection. Even stacking frames with a small standard deviation does not necessarily make it that a detection is assured. Things are more complicated in the reality of dealing with the data for this thesis, as the predicted absorption is $\sim$0.5%, rather than the 2% used in this example. Also, the changes in Earth's atmosphere over short times (even from frame to frame) make it difficult to accurately model the absorption features, increasing the noise in the

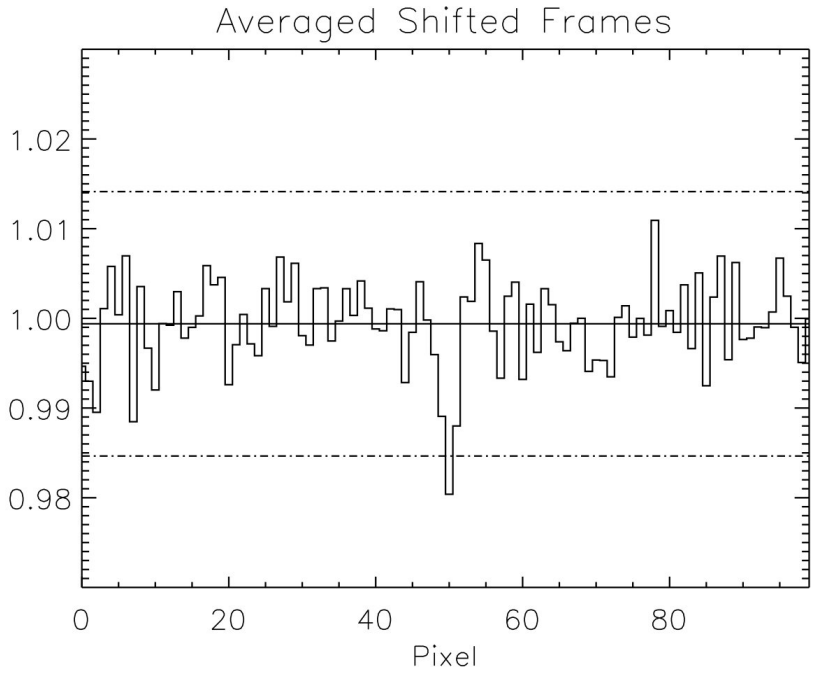

Figure B.4 This shows the shifted and added frames, where there is finally a 3σ detection.

reduced spectrum. Similarly, there can be a S/N "threshold" where the noise from the instrument will cancel any gains made by integrating for a longer time. The best way to counter these limitations is to improve data collection techniques and increase the accuracy of the atmospheric models.

BIBLIOGRAPHY

Beaulieu, J.-P., Bennett, D. P., Fouqué, P., Williams, A., Dominik, M., Jorgensen, U. G., Kubas, D., Cassan, A., Coutures, C., Greenhill, J., Hill, K., Menzies, J., Sackett, P. D., Albrow, M., Brillant, S., Caldwell, J. A. R., Calitz, J. J., Cook, K. H., Corrales, E., Desort, M., Dieters, S., Dominis, D., Donatowicz, J., Hoffman, M., Kane, S., Marquette, J.-B., Martin, R., Meintjes, P., Pollard, K., Sahu, K., Vinter, C., Wambsganss, J., Woller, K., Horne, K., Steele, I., Bramich, D. M., Burgdorf, M., Snodgrass, C., Bode, M., Udalski, A., Szymański, M. K., Kubiak, M., Więckowski, T., Pietrzyński, G., Soszyński, I., Szewczyk, O., Wyrzykowski, Ł., Paczyński, B., Abe, F., Bond, I. A., Britton, T. R., Gilmore, A. C., Hearnshaw, J. B., Itow, Y., Kamiya, K., Kilmartin, P. M., Korpela, A. V., Masuda, K., Matsubara, Y., Motomura, M., Muraki, Y., Nakamura, S., Okada, C., Ohnishi, K., Rattenbury, N. J., Sako, T., Sato, S., Sasaki, M., Sekiguchi, T., Sullivan, D. J., Tristram, P. J., Yock, P. C. M., and Yoshioka, T. 2006. Discovery of a cool planet of 5.5 Earth masses through gravitational microlensing. *Nature 439*, 437–440.

Berriman, G. B., Ciardi, D. R., Good, J. C., Laity, A. C., and Zhang, A. 2006. The NASA Navigator Program Ground Based Archives at the Michelson Science Center: Supporting the Search for Habitable Planets. In *ASP Conf. Ser. 351: Astronomical Data Analysis Software and Systems XV*, C. Gabriel, C. Arviset, D. Ponz, and S. Enrique, Eds. 120–+.

Brittain, S. D. 2004. Using high-resolution near infrared spectroscopy to probe the interstellar medium and circumstellar disks. Ph.D. thesis, AA(UNIVERSITY OF NOTRE DAME).

Brittain, S. D., Rettig, T. W., Simon, T., Kulesa, C., DiSanti, M. A., and Dello Russo, N. 2003. CO Emission from Disks around AB Aurigae and HD 141569: Implications for Disk Structure and Planet Formation Timescales. *Astrophys. J. 588*, 535–544.

Broadfoot, A. L., Belton, M. J., Takacs, P. Z., Sandel, B. R., Shemansky, D. E., Holberg, J. B., Ajello, J. M., Moos, H. W., Atreya, S. K., Donahue, T. M., Bertaux, J. L., Blamont, J. E., Strobel, D. F., McConnell, J. C., Goody, R., Dalgarno, A., and McElroy, M. B. 1979. Extreme ultraviolet observations from Voyager 1 encounter with Jupiter. *Science 204*, 979–982.

Brown, T. M., Charbonneau, D., Gilliland, R. L., Noyes, R. W., and Burrows, A. 2001. Hubble Space Telescope Time-Series Photometry of the Transiting Planet of HD 209458. *Astrophys. J. 552*, 699–709.

Butler, R. P., Wright, J. T., Marcy, G. W., Fischer, D. A., Vogt, S. S., Tinney, C. G., Jones, H. R. A., Carter, B. D., Johnson, J. A., McCarthy, C., and Penny, A. J. 2006. Catalog of Nearby Exoplanets. *Astrophys. J. 646*, 505–522.

Charbonneau, D., Allen, L. E., Megeath, S. T., Torres, G., Alonso, R., Brown, T. M., Gilliland, R. L., Latham, D. W., Mandushev, G., O'Donovan, F. T., and Sozzetti, A. 2005. Detection of Thermal Emission from an Extrasolar Planet. *Astrophys. J. 626*, 523–529.

Charbonneau, D., Brown, T. M., Latham, D. W., and Mayor, M. 2000. Detection of Planetary Transits Across a Sun-like Star. *Astrophys. J. Lett. 529*, L45–L48.

Charbonneau, D., Brown, T. M., Noyes, R. W., and Gilliland, R. L. 2002. Detection of an Extrasolar Planet Atmosphere. *Astrophys. J. 568*, 377–384.

Chauvin, G., Lagrange, A.-M., Dumas, C., Zuckerman, B., Mouillet, D., Song, I., Beuzit, J.-L., and Lowrance, P. 2004. A giant planet candidate near a young brown dwarf. Direct VLT/NACO observations using IR wavefront sensing. *A&A 425*, L29–L32.

Deming, D., Brown, T. M., Charbonneau, D., Harrington, J., and Richardson, L. J. 2005a. A New Search for Carbon Monoxide Absorption in the Transmission Spectrum of the Extrasolar Planet HD 209458b. *Astrophys. J. 622*, 1149–1159.

Deming, D., Seager, S., Richardson, L. J., and Harrington, J. 2005b. Infrared radiation from an extrasolar planet. *Nature 434*, 740–743.

Des Marais, D. J., Harwit, M. O., Jucks, K. W., Kasting, J. F., Lin, D. N. C., Lunine, J. I., Schneider, J., Seager, S., Traub, W. A., and Woolf, N. J. 2002. Remote Sensing of Planetary Properties and Biosignatures on Extrasolar Terrestrial Planets. *Astrobiology 2*, 153–181.

Fischer, D. A. and Valenti, J. 2005. The Planet-Metallicity Correlation. *Astrophys. J. 622*, 1102–1117.

Fortney, J. J., Saumon, D., Marley, M. S., Lodders, K., and Freedman, R. S. 2006. Atmosphere, Interior, and Evolution of the Metal-rich Transiting Planet HD 149026b. *Astrophys. J. 642*, 495–504.

Geballe, T. R., Jagod, M.-F., and Oka, T. 1992. Saturn. *IAU Circ. 5566*, 2–+.

Goto, M., McCall, B. J., Geballe, T. R., Usuda, T., Kobayashi, N., Terada, H., and Oka, T. 2002. Absorption Line Survey of H3+ toward the Galactic Center Sources I. GCS 3-2 and GC IRS3. *PASJ 54*, 951–961.

Henry, G. W., Marcy, G. W., Butler, R. P., and Vogt, S. S. 2000. A Transiting "51 Peg-like" Planet. *Astrophys. J. Lett. 529*, L41–L44.

Knutson, H. A., Charbonneau, D., Noyes, R. W., Brown, T. M., and Gilliland, R. L. 2007. Using Stellar Limb-Darkening to Refine the Properties of HD 209458b. *Astrophys. J. 655*, 564–575.

Kunde, V. R. and Maguire, W. C. 1974. Direct integration transmittance model. *Journal of Quantitative Spectroscopy and Radiative Transfer 14*, 803–817.

Lindsay, C. M. and McCall, B. J. 2001. Comprehensive Evaluation and Compilation of H 3 + Spectroscopy. *Journal of Molecular Spectroscopy 210*, 60–83.

Marley, M. S., Fortney, J., Seager, S., and Barman, T. 2007. Atmospheres of Extrasolar Giant Planets. In *Protostars and Planets V*, B. Reipurth, D. Jewitt, and K. Keil, Eds. 733–747.

Mayor, M. and Queloz, D. 1995. A Jupiter-Mass Companion to a Solar-Type Star. *Nature 378*, 355–+.

Mazeh, T., Naef, D., Torres, G., Latham, D. W., Mayor, M., Beuzit, J.-L., Brown, T. M., Buchhave, L., Burnet, M., Carney, B. W., Charbonneau, D., Drukier, G. A., Laird, J. B., Pepe, F., Perrier, C., Queloz, D., Santos, N. C., Sivan, J.-P., Udry, S., and Zucker, S. 2000. The Spectroscopic Orbit of the Planetary Companion Transiting HD 209458. *Astrophys. J. Lett. 532*, L55–L58.

McCall, B. J. 2001. Spectroscopy of trihydrogen(+) in laboratory and astrophysical plasmas. Ph.D. thesis, AA(Department of Chemistry and Department of Astronomy and Astrophysics, University of Chicago, 5735 S. Ellis Ave., Chicago, IL 60637.

McCall, B. J., Geballe, T. R., Hinkle, K. H., and Oka, T. 1999. Observations of H^+_3 in Dense Molecular Clouds. *Astrophys. J. 522*, 338–348.

Melin, H., Miller, S., Stallard, T., and Grodent, D. 2005. Non-LTE effects on H3+ emission in the jovian upper atmosphere. *Icarus 178*, 97–103.

Melo, C., Santos, N. C., Pont, F., Guillot, T., Israelian, G., Mayor, M., Queloz, D., and Udry, S. 2006. On the age of stars harboring transiting planets. *A&A 460*, 251–256.

Miller, S., Achilleos, N., Ballester, G. E., Geballe, T. R., Joseph, R. D., Prangé, R., Rego, D., Stallard, T., Tennyson, J., Trafton, L. M., and Waite, Jr., J. H. 2000. The role of H_3^+ in planetary atmospheres. In *Astronomy, physics and chemistry of H_3^+*. 2485–+.

Miller, S., Joseph, R. D., and Tennyson, J. 1990. Infrared emissions of H3(+) in the atmosphere of Jupiter in the 2.1 and 4.0 micron region. *Astrophys. J. Lett. 360*, L55–L58.

Montes, D., López-Santiago, J., Gálvez, M. C., Fernández-Figueroa, M. J., De Castro, E., and Cornide, M. 2001. Late-type members of young stellar kinematic groups - I. Single stars. *MNRAS 328*, 45–63.

Moutou, C., Coustenis, A., Schneider, J., St Gilles, R., Mayor, M., Queloz, D., and Kaufer, A. 2001. Search for spectroscopical signatures of transiting HD 209458b's exosphere. *A&A 371*, 260–266.

Rothman, L. S., Gamache, R. R., Tipping, R. H., Rinsland, C. P., Smith, M. A. H., Benner, D. C., Devi, V. M., Flaud, J.-M., Camy-Peyret, C., and Perrin, A. 1992. The HITRAN molecular data base - Editions of 1991 and 1992. *Journal of Quantitative Spectroscopy and Radiative Transfer 48*, 469–507.

Rothman, L. S., Rinsland, C. P., Goldman, A., Massie, S. T., Edwards, D. P., Flaud, J.-M., Perrin, A., Camy-Peyret, C., Dana, V., Mandin, J.-Y., Schroeder, J., McCann, A., Gamache, R. R., Wattson, R. B., Yoshino, K., Chance, K., Jucks, K., Brown, L. R., Nemtchinov, V., and Varanasi, P. 1998. The HITRAN Molecular Spectroscopic Database and HAWKS (HITRAN Atmospheric Workstation): 1996 Edition. *Journal of Quantitative Spectroscopy and Radiative Transfer 60*, 665–710.

Seager, S. and Sasselov, D. D. 2000. Theoretical Transmission Spectra during Extrasolar Giant Planet Transits. *Astrophys. J. 537*, 916–921.

Selsis, F. 2002. Search for signatures of life on exoplanets. In *ESA SP-514: Earth-like Planets and Moons*, B. H. Foing and B. Battrick, Eds. 251–258.

Shkolnik, E., Gaidos, E., and Moskovitz, N. 2006. No Detectable H_3^+ Emission from the Atmospheres of Hot Jupiters. *Astrophysical Journal 132*, 1267–1274.

Sidhu, K. S., Miller, S., and Tennyson, J. 1992. Partition functions and equilibrium constants for H3+ and H2D+. *A&A 255*, 453–456.

Trafton, L. M., Geballe, T. R., Miller, S., Tennyson, J., and Ballester, G. E. 1993. Detection of H3(+) from Uranus. *Astrophys. J. 405*, 761–766.

VanLoon, G. W. 2000. *Environmental chemistry : a global perspective*. ISBN 0198564414. Oxford University Press, 2000.

Vidal-Madjar, A., Désert, J.-M., Lecavelier des Etangs, A., Hébrard, G., Ballester, G. E., Ehrenreich, D., Ferlet, R., McConnell, J. C., Mayor, M., and Parkinson, C. D. 2004. Detection of Oxygen and Carbon in the Hydrodynamically Escaping Atmosphere of the Extrasolar Planet HD 209458b. *Astrophys. J. Lett. 604*, L69–L72.

Vidal-Madjar, A. and Etangs, A. L. D. 2004. "Osiris"(HD209458b), an Evaporating Planet. In *ASP Conf. Ser. 321: Extrasolar Planets: Today and Tomorrow*, J. Beaulieu, A. Lecavelier Des Etangs, and C. Terquem, Eds. 152–+.

Vidal-Madjar, A., Lecavelier des Etangs, A., Désert, J.-M., Ballester, G. E., Ferlet, R., Hébrard, G., and Mayor, M. 2003. An extended upper atmosphere around the extrasolar planet HD209458b. *Nature 422*, 143–146.

Winn, J. N., Noyes, R. W., Holman, M. J., Charbonneau, D., Ohta, Y., Taruya, A., Suto, Y., Narita, N., Turner, E. L., Johnson, J. A., Marcy, G. W., Butler, R. P., and Vogt, S. S. 2005. Measurement of Spin-Orbit Alignment in an Extrasolar Planetary System. *Astrophys. J. 631*, 1215–1226.

Wittenmyer, R. A., Welsh, W. F., Orosz, J. A., Schultz, A. B., Kinzel, W., Kochte, M., Bruhweiler, F., Bennum, D., Henry, G. W., Marcy, G. W., Fischer, D. A., Butler, R. P., and Vogt, S. S. 2005. System Parameters of the Transiting Extrasolar Planet HD 209458b. *Astrophys. J. 632*, 1157–1167.

Wolszczan, A. and Frail, D. A. 1992. A planetary system around the millisecond pulsar PSR1257 + 12. *Nature 355*, 145–147.

Yelle, R. V. 2004. Aeronomy of extra-solar giant planets at small orbital distances. *Icarus 170*, 167–179.